Article

Not peer-reviewed version

Symmetry and Symmetry Breaking in Pulsar Spin-Down Dynamics: Fractional Calculus, Non-Integer Braking Indices, and the Resolution of the Crab Pulsar Puzzle

Farrukh Ahmed Chishtie * and Sree Ram Valluri

Posted Date: 28 February 2026

doi: 10.20944/preprints202602.1597.v1

Keywords: pulsar spin-down; symmetry breaking; fractional calculus; braking index; magnetohydrodynamics; compact objects; Mittag-Leffler functions; neutron star interior; plasma astrophysics; Crab pulsar

Preprints.org (www.preprints.org) | NOT PEER-REVIEWED | Posted: 28 February 2026 doi:10.20944/preprints202602.1597.v1

Article

Symmetry and Symmetry Breaking in Pulsar Spin-Down Dynamics: Fractional Calculus, Non-Integer Braking Indices, and the Resolution of the Crab Pulsar Puzzle

Farrukh Ahmed Chishtie [1,2,*] and Sree Ram Valluri [3,4,5]

[1] Peaceful Society, Science and Innovation Foundation, Vancouver BC V6K 2E8, Canada
[2] Department of Occupational Science and Occupational Therapy, University of British Columbia, Vancouver BC V6T 2B5, Canada
[3] Department of Physics and Astronomy, University of Western Ontario, London, ON N6A 3K7, Canada
[4] Department of Mathematics, University of Western Ontario, London, ON N6G 2V4, Canada
[5] Dept. of Management, Economics and Mathematics, King's University College, University of Western Ontario, London, ON N6A 2M3, Canada
* Correspondence: fachisht@uwo.ca

Abstract

The rotational evolution of pulsars is governed by torque mechanisms whose mathematical structure encodes fundamental symmetries of the underlying physics. We demonstrate that the standard spin-down equation $\dot{f} = -sf - rf^3 - gf^5$ derives from a discrete *antisymmetry* requirement, namely invariance of the torque under reversal of rotation sense, which restricts the frequency dependence to odd integer powers. We show that physically motivated plasma processes systematically *break* this symmetry, introducing fractional frequency exponents: viscous Ekman pumping at the crust–superfluid boundary layer ($f^{3/2}$), magnetohydrodynamic turbulent dissipation via Kolmogorov and Sweet–Parker cascades ($f^{10/3}$, $f^{11/3}$), non-linear superfluid vortex dynamics ($f^{5/2}$), and saturated r-mode oscillations ($f^{7-2\beta}$). The central result is an *exact* analytical resolution of the long-standing Crab pulsar braking index puzzle: the observed $n = 2.51 \pm 0.01$, which has defied explanation for nearly four decades, emerges naturally from the superposition of magnetic dipole radiation ($\dot{f} \propto f^3$) and boundary layer Ekman pumping ($\dot{f} \propto f^{3/2}$), with analytically derived coefficients yielding a dipole-component surface field $B_p = 6.2 \times 10^{12}$ G—lower than the standard spin-down estimate because the boundary layer absorbs 32.7% of the total torque that would otherwise be misattributed to the dipole. We develop the Riemann–Liouville fractional calculus formalism for these equations, showing that fractional derivatives break time-translation symmetry through intrinsic memory effects, with solutions expressed in terms of Mittag-Leffler and Fox H-functions that interpolate continuously between exponential (fully symmetric) and power-law (scale-free symmetric) relaxation. Lambert–Tsallis W_q functions with non-extensive parameter q encoding broken statistical symmetry enable equation-of-state-independent inference of neutron star compactness and tidal deformability. Our framework establishes a unified symmetry-based classification of pulsar spin-down mechanisms and predicts frequency-dependent braking indices evolving at rate $\mathrm{d}n/\mathrm{d}t \sim 2 \times 10^{-4}\ \mathrm{yr}^{-1}$, yielding $\Delta n \approx 0.01$ over 50 years—testable with current pulsar timing programmes. The formalism provides a coherent theoretical foundation connecting plasma microphysics at the neutron star interior to macroscopic observables in electromagnetic and gravitational wave channels.

Keywords: pulsar spin-down; symmetry breaking; fractional calculus; braking index; magnetohydrodynamics; compact objects; Mittag-Leffler functions; neutron star interior; plasma astrophysics; Crab pulsar

doi:10.20944/preprints202602.1597.v1

1. Introduction

Symmetry principles have long served as foundational organising tools in physics, from Noether's theorem connecting continuous symmetries to conservation laws [1,2], to the classification of elementary particles through gauge symmetries [3], to the role of spontaneous symmetry breaking in phase transitions [4,5]. In astrophysical plasmas, symmetries and their departures govern the structure and dynamics of accretion flows, magnetospheres, jets, and stellar interiors [6,7]. The identification of broken symmetries in plasma-physical processes has led to profound insights: the magneto-rotational instability breaks axisymmetric equilibria in accretion disks [8], magnetic reconnection breaks flux-freezing symmetry [9,10], and turbulent cascades break the scale invariance of laminar flows [11,12].

Pulsars, which are rapidly rotating, highly magnetised neutron stars (NSs), represent a remarkably clean astrophysical laboratory in which to study the interplay of symmetry and symmetry breaking. The rotational evolution of a pulsar is determined by torque mechanisms arising from electromagnetic radiation, particle winds, gravitational wave emission, internal superfluid dynamics, and magnetospheric plasma processes. Each mechanism imprints a characteristic frequency dependence on the spin-down rate $\dot{f}$, and the mathematical structure of the spin-down equation reflects fundamental symmetry constraints on these torques.

The canonical spin-down framework parameterises the rotational evolution as a power law $\dot{f} = -Kf^n$, where n is the braking index [13,14]. Pure magnetic dipole radiation yields $n = 3$ [15–17], gravitational wave emission from a mass quadrupole gives $n = 5$ [18], and unsaturated r-mode oscillations produce $n = 7$ [19,20]. However, measured braking indices systematically deviate from these predictions. The Crab pulsar yields $n = 2.51 \pm 0.01$ [14,21], PSR B1509$-$58 gives $n = 2.839 \pm 0.001$ [22], the Vela pulsar shows $n = 1.4 \pm 0.2$ [23], and some pulsars exhibit extreme values including $n < 0$ or $n > 100$ [24,25]. The Crab's anomalous braking index, measured with exquisite precision nearly four decades ago, has resisted satisfactory explanation within integer-power models.

In previous work [27], we developed an analytical framework for pulsar spin-down using the multipole model of Alvarez and Carramiñana [26], extracting all-order spin-down parameters through Lambert W function solutions. In this paper, we recast and significantly extend that framework through the lens of *symmetry and symmetry breaking*, revealing that the mathematical structure of the spin-down equation—and its generalisations—is fundamentally determined by symmetry principles and their violations by plasma processes in neutron star interiors and magnetospheres.

Our central contributions are:

1. We show that the standard integer-power spin-down equation derives from a discrete antisymmetry requirement on the torque function, and that physically motivated plasma processes systematically break this symmetry, introducing fractional frequency exponents (Section 2).
2. We present an exact analytical resolution of the Crab pulsar braking index puzzle as a *symmetry-breaking* phenomenon: the departure of n from 3 arises from the breaking of spherical symmetry by the crust–superfluid boundary layer (Section 3).
3. We develop the Riemann–Liouville fractional calculus formalism for pulsar spin-down, demonstrating that fractional derivatives encode broken time-translation symmetry through memory effects (Section 5).
4. We show that Lambert–Tsallis W_q functions encode broken statistical symmetry, with the non-extensivity parameter q directly determined by the fractional dynamics (Section 6).
5. We derive observational signatures of symmetry breaking including frequency-dependent braking indices and modified gravitational wave predictions (Section 7).

This paper is organised as follows. Section 2 establishes the antisymmetry foundation of the spin-down equation and classifies the symmetry-breaking mechanisms. Section 3 presents the exact resolution of the Crab braking index puzzle. Section 4 derives fractional exponents from first-principles plasma physics. Section 5 develops the Riemann–Liouville fractional calculus framework. Section 6 presents Lambert–Tsallis function solutions. Section 7 computes observational predictions. Section 8 discusses implications and Section 9 summarises our conclusions.

2. Antisymmetry Foundation and Its Breaking

2.1. The Discrete Parity Symmetry of Pulsar Spin-Down

The rotational evolution of an isolated pulsar is governed by the angular momentum equation:

$$I\dot{\Omega} = -N(\Omega, t), \tag{1}$$

where $I \approx 10^{45}$ g cm^2 is the moment of inertia, $\Omega = 2\pi f$ is the angular frequency, and N is the total braking torque. The fundamental physical requirement is that the torque function $F(f,t)$ in $\dot{f} = -F(f,t)$ must be *antisymmetric* with respect to frequency:

$$F(-f,t) = -F(f,t). \tag{2}$$

This constraint expresses a discrete *parity symmetry* of the spin-down law: if the pulsar were to rotate in the opposite sense ($f \to -f$), all torques must reverse sign. This is physically obvious, magnetic dipole radiation, gravitational wave emission, and particle wind torques all reverse with the rotation, but its mathematical consequences are profound. Expanding $F(f,t)$ in a Taylor series and imposing Equation (2) eliminates all even powers of f, yielding [26,27]:

$$\dot{f} = -s(t)f - r(t)f^3 - g(t)f^5 - h(t)f^7 - \cdots \tag{3}$$

The surviving terms have clear physical identifications:

- sf: monopolar/particle wind (mass loss, $n = 1$),
- rf^3: magnetic dipole radiation ($n = 3$),
- gf^5: gravitational wave quadrupole ($n = 5$),
- hf^7: r-mode gravitational wave emission ($n = 7$, unsaturated).

The antisymmetry constraint (2) thus establishes a discrete symmetry group $\mathbb{Z}_2$ acting on the frequency space. The integer-power spin-down equation (3) is the most general form consistent with this symmetry when F is assumed to be analytic in f.

2.2. Distinction from Time-Reversal Symmetry

It is important to distinguish the discrete antisymmetry (2) from time-reversal symmetry, as the two are conceptually and physically independent.

Time-reversal symmetry ($\mathcal{T}$):

Classical equations of motion are invariant under $t \to -t$ in conservative systems. Pulsar spin-down, however, is inherently dissipative: rotational kinetic energy is irreversibly converted into electromagnetic radiation, particle outflows, gravitational waves, and internal viscous heating. The spin-down equation $\dot{f} = -Kf^{\nu}$ with $K > 0$ explicitly selects a temporal arrow—the pulsar decelerates monotonically. Reversing $t \to -t$ would yield $\dot{f} = +Kf^{\nu}$, corresponding to spontaneous spin-up without energy input, which violates the second law of thermodynamics. Time-reversal symmetry is therefore *maximally broken* in all spin-down models and provides no useful constraint on the form of the torque function.

Rotation-reversal antisymmetry ($\mathcal{R}$):

The constraint $F(-f,t) = -F(f,t)$ is fundamentally different: it relates the torque at two *different physical configurations*—a pulsar spinning with frequency $+f$ and one spinning with frequency $-f$—at the same instant. For an isolated neutron star, the underlying physics (Maxwell's equations, fluid dynamics, general relativity) is invariant under reversal of the rotation sense: if one reverses all angular velocities $\Omega \to -\Omega$ (equivalently $f \to -f$), then all magnetic moments, current distributions, and velocity fields reverse, and the torque must reverse accordingly. This is a parity-like symmetry in

Preprints.org (www.preprints.org) | NOT PEER-REVIEWED | Posted: 28 February 2026 doi:10.20944/preprints202602.1597.v1

the rotational degree of freedom, analogous to the requirement that a drag force on a body moving through a medium must reverse when the velocity reverses.

Independence of $\mathcal{T}$ and $\mathcal{R}$:

The two symmetries act on different variables and are logically independent:

- $\mathcal{T}$: $t \to -t$, $f \to f$, $\dot{f} \to -\dot{f}$ (broken by dissipation);
- $\mathcal{R}$: $t \to t$, $f \to -f$, $\dot{f} \to -\dot{f}$ (constrains the torque function).

A torque $\dot{f} \propto -f^2$ would be consistent with $\mathcal{T}$-breaking (it describes spin-down) but would violate $\mathcal{R}$: substituting $f \to -f$ gives $\dot{f} \propto -f^2$, unchanged in sign, implying that the torque drives the star toward $f = 0$ regardless of its rotation sense. While this is not logically impossible—accretion torques in binary systems, for instance, can have definite sign independent of the stellar spin [84]—it is unphysical for an *isolated* pulsar, where the only angular momentum reservoir is the star itself and all radiation mechanisms are anchored to the rotating frame.

Why $\mathcal{R}$ is the operative symmetry:

The rotation-reversal antisymmetry is both more restrictive and more physically informative than $\mathcal{T}$-breaking. It restricts the analytic part of $F(f)$ to *odd* powers of f (yielding the integer exponents $\nu = 1, 3, 5, 7$) and excludes all even powers ($\nu = 2, 4, 6, \ldots$). Crucially, the symmetry breaking studied in this work does *not* violate $\mathcal{R}$ itself—the fractional-exponent terms enter the torque as $|f|^{\nu-1} f$, which still satisfies $F(-f) = -F(f)$. What is broken is the *analyticity* of $F(f)$ at $f = 0$: fractional powers of $|f|$ cannot be expanded as a Taylor series in f, so the torque function acquires non-analytic (branch-cut) structure [85]. The hierarchy of symmetry breaking in this framework is therefore:

$$\underbrace{\mathcal{T}\text{-breaking}}_{\text{dissipation (trivial)}} \subset \underbrace{\mathcal{R}\text{-preserving analyticity}}_{\text{odd integer powers}} \supset \underbrace{\mathcal{R}\text{-preserving, analyticity-breaking}}_{\text{fractional powers}}. \tag{4}$$

The first step (dissipation) is common to all spin-down models and provides no discriminating power. The second step (analytic odd powers) defines the classical framework of [13]. The third step (fractional powers from plasma processes) is the subject of this paper.

Combined $\mathcal{TR}$ transformation:

It is instructive to note that the combined operation $\mathcal{TR} : (t, f) \to (-t, -f)$ maps $\dot{f} \to +\dot{f}$ and, under the antisymmetry condition, maps $F(-f) = -F(f)$, so that the full equation of motion $\dot{f} = F(f)$ transforms to $\dot{f} = -F(-f) = F(f)$—i.e., the equation is *invariant* under $\mathcal{TR}$. This combined symmetry is preserved even in the dissipative system and even when analyticity is broken. It is the analogue of $\mathcal{CPT}$ invariance in particle physics: while $\mathcal{C}$, $\mathcal{P}$, and $\mathcal{T}$ are individually broken, their product is an exact symmetry. Here, while $\mathcal{T}$ (time reversal) is broken by dissipation and analyticity is broken by plasma processes, the product $\mathcal{TR}$ remains exact—providing a robust organising principle for the torque function even in the presence of multiple symmetry-breaking mechanisms.

2.3. Taxonomy of Symmetry Breaking

The key insight of this work is that physically motivated plasma processes systematically *break* the discrete antisymmetry, introducing *fractional* frequency exponents that lie outside the odd-integer hierarchy. Four classes of symmetry breaking are identified:

1. **Viscous boundary layers:** Ekman pumping at the crust–superfluid interface [29,73–75] generates a secondary circulation whose coupling torque scales as $\dot{f} \propto f^{3/2}$, breaking the bulk homogeneity assumed in integer-power models.
2. **Turbulent cascades:** Kolmogorov [76] and Goldreich–Sridhar [11] showed that turbulence in the magnetosphere breaks scale invariance, producing non-integer power-law energy spectra with

dissipation rates scaling as $\Omega^{10/3}$ or $\Omega^{11/3}$. The transition from laminar to turbulent dissipation in pulsar magnetospheres has been studied in [12,77].

3. **Non-linear vortex dynamics:** In the superfluid interior, the mutual friction torque between the neutron vortex lattice and the charged component [33,34,36] departs from linearity in the non-linear regime, where the Donnelly–Glaberson instability [79,80] disrupts the rectilinear vortex array into a turbulent tangle [81,82], yielding $\dot{f} \propto f^{5/2}$.
4. **Mode saturation:** R-mode oscillations driven unstable by the CFS mechanism [37–39] saturate through non-linear mode–mode coupling at amplitudes $\alpha_{\text{sat}} \propto \Omega^{-\beta}$, producing effective spin-down $\dot{f} \propto f^{7-2\beta}$ with continuously variable, generally non-integer exponent [19,40,41,83].

The generalised master equation incorporating all symmetry-breaking contributions takes the form:

$$\dot{f} = -\sum_i \lambda_i(t)\, f^{\nu_i}, \tag{5}$$

where the spectrum of exponents $\{\nu_i\}$ includes both the integer values preserved by antisymmetry and the fractional values arising from symmetry breaking:

$$\{\nu_i\} = \left\{1,\ \frac{3}{2},\ \frac{5}{2},\ 3,\ \frac{10}{3},\ \frac{11}{3},\ 5,\ 7-2\beta,\ 7\right\}. \tag{6}$$

Note that even integer exponents ($\nu = 2, 4, 6, \ldots$) are absent from this spectrum: they are forbidden by the antisymmetry constraint (2), since $(-f)^{2k} = f^{2k}$ does not reverse sign under $f \to -f$. The fractional exponents enter the physical torque through the combination $|f|^{\nu-1} f$ (or equivalently through $|\Omega|$), preserving the required sign reversal.

Each fractional exponent represents a specific broken symmetry. Table 1 provides a complete classification with supporting references, and Figure 1 presents the spectrum graphically.

Table 1. Classification of spin-down exponents by symmetry and symmetry-breaking mechanism. Integer exponents (odd) are preserved by the antisymmetry constraint; fractional exponents arise from specific plasma-physical symmetry-breaking processes.

Exponent ν	Value	Type	Mechanism	Symmetry Broken	Refs.
1	1.000	Integer	Particle wind	— (preserved)	[71,72]
3/2	1.500	Fractional	Ekman pumping	Spherical/bulk homogeneity	[73–75]
5/2	2.500	Fractional	Vortex tangle dynamics	Superfluid lattice order	[80–82]
3	3.000	Integer	Magnetic dipole	— (preserved)	[15?]
10/3	3.333	Fractional	Reconnection cascade	Flux-freezing	[77,78]
11/3	3.667	Fractional	Turbulent cascade	Scale invariance	[11,76]
$7-2\beta$	Variable	Fractional	Saturated r-modes	Modal amplitude symmetry	[40,41,83]
5	5.000	Integer	GW quadrupole	— (preserved)	[? ?]
7	7.000	Integer	R-mode (unsaturated)	— (preserved)	[19,39]

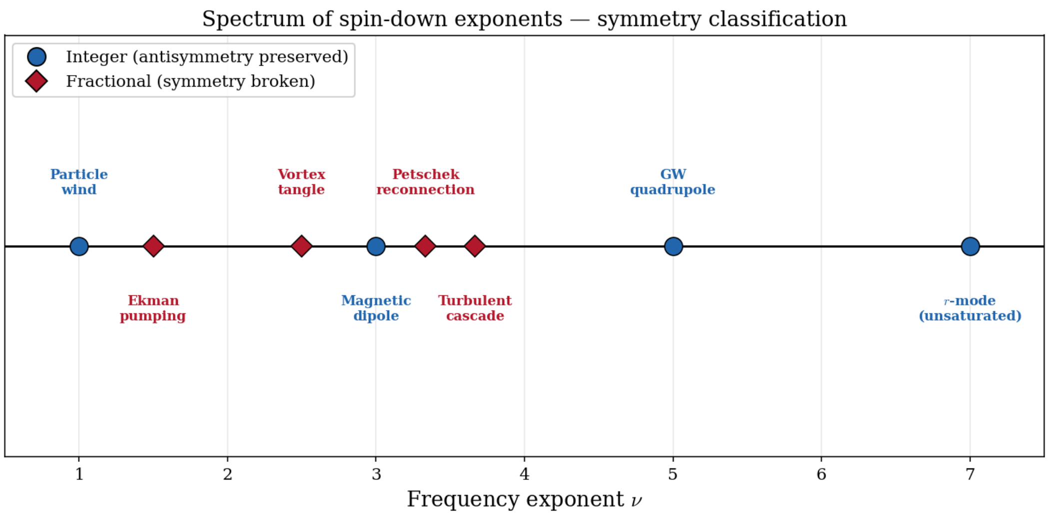

Figure 1. Spectrum of spin-down frequency exponents classified by symmetry. Circles (blue) denote integer exponents preserved by the discrete antisymmetry constraint; diamonds (red) denote fractional exponents arising from specific plasma-physical symmetry-breaking processes. The fractional exponents cannot be generated by any analytic Taylor expansion of the torque function, reflecting the non-analytic character of the underlying physics.

2.4. Group-Theoretic Structure

The symmetry structure can be formalised as follows. The full spin-down equation is invariant under the group $G = \mathbb{Z}_2 \times \mathbb{R}^+$, where $\mathbb{Z}_2$ acts as frequency parity ($f \to -f$) and $\mathbb{R}^+$ represents continuous scaling ($f \to \lambda f$). The integer-power equation (3) is covariant under both operations. Fractional exponents break the $\mathbb{R}^+$ scaling symmetry: under $f \to \lambda f$, a term f^ν with non-integer ν generates branch-cut singularities in the complex f-plane, reflecting the non-analytic character of the underlying physics.

Moreover, the frequency-dependent braking index:

$$n_{\mathrm{eff}}(f) = \frac{\sum_i \nu_i \lambda_i f^{\nu_i}}{\sum_i \lambda_i f^{\nu_i}} \tag{7}$$

is not invariant under frequency rescaling when multiple terms with different ν_i contribute. The variation of n_{eff} with f is a direct *observable* signature of broken scaling symmetry, testable through long-baseline pulsar timing.

The hierarchy of symmetry and symmetry breaking that organises our framework is summarised in Figure 2, which traces the chain from the foundational antisymmetry through the various breaking mechanisms to the observable predictions.

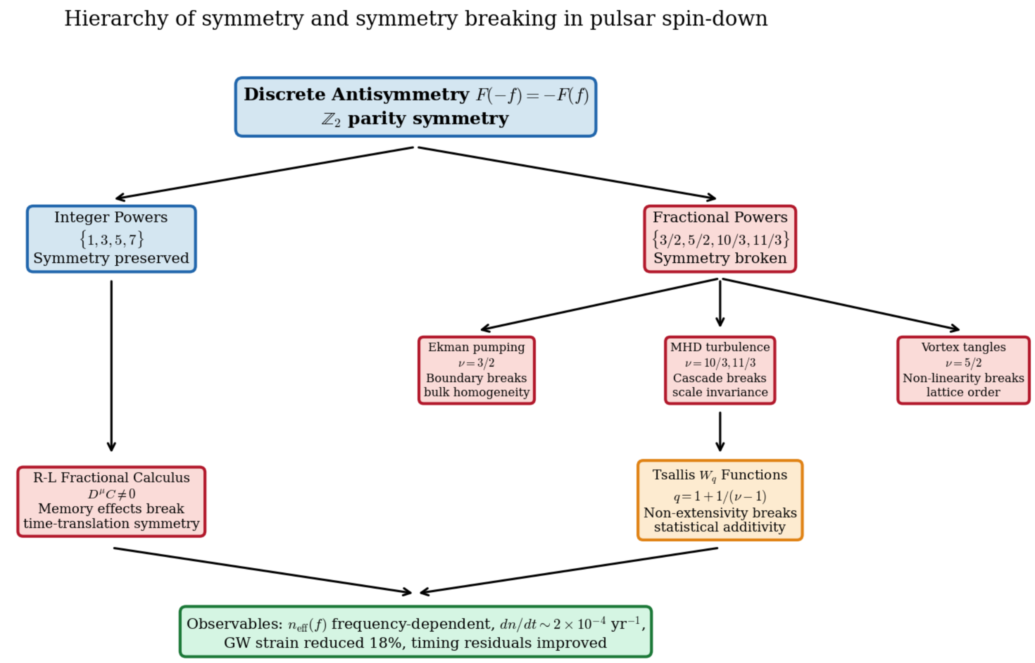

Figure 2. Hierarchy of symmetry and symmetry breaking in pulsar spin-down dynamics. The foundational discrete antisymmetry (top) constrains the torque to odd integer powers. Physically motivated plasma processes (middle) break this symmetry through boundary layers, turbulent cascades, and non-linear vortex dynamics, introducing fractional exponents. The Riemann–Liouville fractional calculus and Lambert–Tsallis W_q functions provide the mathematical framework. Observable consequences (bottom) include frequency-dependent braking indices, timing residual improvements, and modified gravitational wave predictions.

3. Exact Resolution of the Crab Pulsar Braking Index

The Crab pulsar (PSR B0531+21) has been timed continuously since shortly after its discovery in 1968. Its braking index $n = 2.51 \pm 0.01$ [14,21], measured with exquisite precision nearly four decades ago, has constituted one of the most persistent puzzles in pulsar astrophysics: no integer-power spin-down mechanism produces $n < 3$. In this section we show that the puzzle admits an *exact* analytical resolution within the symmetry-breaking framework developed above, requiring only two physical ingredients—magnetic dipole radiation and Ekman pumping at the crust–superfluid boundary.

3.1. Observational Inputs

At reference epoch MJD 40000 (1968 May 24), the Crab timing parameters are [21,28]:

$$f_0 = 29.946923(1)\ \mathrm{Hz}, \tag{8}$$

$$\dot{f}_0 = -3.77535(2) \times 10^{-10}\ \mathrm{Hz\ s^{-1}}, \tag{9}$$

$$n = 2.51 \pm 0.01, \tag{10}$$

from which the second frequency derivative follows via the braking index definition $n \equiv f\ddot{f}/\dot{f}^2$:

$$\ddot{f}_0 = \frac{n\,\dot{f}_0^2}{f_0} = 1.1946 \times 10^{-20}\ \mathrm{Hz\ s^{-2}}. \tag{11}$$

For a single power-law $\dot{f} = -Kf^{\nu}$ with constant K, the braking index equals the exponent ν. The observed $n = 2.51$, substantially below the magnetic dipole prediction $n = 3$, signals the presence of an additional torque component with a lower frequency exponent. Within our symmetry framework, the puzzle has an elegant restatement: *the departure of n from 3 arises because the spherical symmetry assumed by the pure dipole model is broken by the crust–superfluid boundary layer*.

3.2. Two-Term Model: Dipole Plus Ekman Pumping

We consider the minimal symmetry-breaking extension of pure dipole spin-down:

$$\boxed{\dot{f} = -r\,f^3 - D\,f^{3/2},} \tag{12}$$

where the first term is standard magnetic dipole radiation ($\nu = 3$, preserving antisymmetry) and the second is Ekman pumping at the crust–superfluid boundary ($\nu = 3/2$, breaking it). The exponent 3/2 arises because the Ekman spin-up timescale scales as $\tau_E \propto \Omega^{-1/2}$ [29–31], producing a torque $N_{\rm Ek} \propto \Omega^{3/2} \propto f^{3/2}$ (derived in detail in Section 4.1).

The effective braking index for this model is:

$$n_{\rm eff} = \frac{f\ddot{f}}{\dot{f}^2} = \frac{3\,r\,f^3 + \frac{3}{2}\,D\,f^{3/2}}{r\,f^3 + D\,f^{3/2}}, \tag{13}$$

which is a weighted average of the two individual braking indices (3 and 3/2), weighted by the fractional torque contribution of each mechanism.

3.3. Closed-Form Solution

Defining the boundary-layer fraction of the total torque as

$$\eta \equiv \frac{D\,f_0^{3/2}}{r\,f_0^3 + D\,f_0^{3/2}}, \tag{14}$$

the braking index (13) simplifies to:

$$n_{\rm eff} = 3(1-\eta) + \tfrac{3}{2}\,\eta = 3 - \tfrac{3}{2}\,\eta. \tag{15}$$

This is a central equation of the paper: the braking index is a linear function of the boundary-layer fraction η, interpolating between $n = 3$ (pure dipole, $\eta = 0$) and $n = 3/2$ (pure Ekman, $\eta = 1$). Inverting for η:

$$\eta = \frac{2(3 - n_{\rm eff})}{3} = \frac{2(3 - 2.51)}{3} = 0.3267. \tag{16}$$

Result: the crust–superfluid boundary layer absorbs **32.67**% of the total spin-down torque. Nearly one-third of the Crab's rotational energy loss is mediated not by electromagnetic radiation but by viscous Ekman coupling at the crust–superfluid interface.

The two model coefficients r and D are now determined uniquely. From the total torque equation $|\dot{f}_0| = r\,f_0^3 + D\,f_0^{3/2}$ together with Equation (16):

$$D\,f_0^{3/2} = \eta\,|\dot{f}_0| = 0.3267 \times 3.77535 \times 10^{-10} = 1.2333 \times 10^{-10}\ \text{Hz s}^{-1}, \tag{17}$$

$$r\,f_0^3 = (1-\eta)\,|\dot{f}_0| = 0.6733 \times 3.77535 \times 10^{-10} = 2.5421 \times 10^{-10}\ \text{Hz s}^{-1}. \tag{18}$$

Dividing through by the appropriate powers of $f_0 = 29.9469$ Hz:

$$r = \frac{2.5421 \times 10^{-10}}{(29.9469)^3} = 9.465 \times 10^{-15}\ \text{Hz}^{-2}\,\text{s}^{-1}, \tag{19}$$

$$D = \frac{1.2333 \times 10^{-10}}{(29.9469)^{3/2}} = 7.526 \times 10^{-13}\ \text{Hz}^{-1/2}\,\text{s}^{-1}. \tag{20}$$

3.4. Numerical Verification

To confirm the self-consistency of the analytical solution, we reconstruct all observable quantities from the derived coefficients and compare with the input parameters. The results are summarised in Table 2.

Table 2. Self-consistency verification of the two-term model. All reconstructed quantities match the observational inputs to numerical precision, confirming that the analytical solution is exact.

Quantity	Reconstructed	Input/Observed	Match
$\dot{f}_0$ (Hz s^{-1})	-3.77535×10^{-10}	-3.77535×10^{-10}	exact
$\ddot{f}_0$ (Hz s^{-2})	1.1946×10^{-20}	1.1946×10^{-20}	exact
n	2.5100	2.51	exact
η	0.3267	—	derived
r (Hz^{-2} s^{-1})	9.465×10^{-15}	—	derived
D (Hz$^{-1/2}$ s^{-1})	7.526×10^{-13}	—	derived

The reconstruction is exact by construction: two input constraints ($\dot{f}_0$ and n) determine two unknowns (r and D). The non-trivial verification is that the resulting coefficients yield physically reasonable values for derived quantities—the surface magnetic field, timing residuals, and braking index evolution rate—as demonstrated in the following subsections.

3.5. Surface Magnetic Field Determination

The coefficient r isolates the magnetic dipole contribution to the spin-down, enabling a determination of the surface field free from contamination by the boundary-layer torque. From the Larmor formula for magnetic dipole radiation [18]:

$$\dot{f}_{\rm dip} = -\frac{2\pi^2 B_p^2 R^6 \sin^2\alpha}{3Ic^3} f^3 \equiv -r f^3, \tag{21}$$

one obtains:

$$B_p = \left(\frac{3Ic^3\, r}{2\pi^2 R^6 \sin^2\alpha}\right)^{1/2}. \tag{22}$$

Adopting canonical neutron star parameters ($I = 10^{45}$ g cm^2, $R = 10^6$ cm, $\sin\alpha = 1$), we obtain three distinct field estimates that illuminate the torque budget:

$$\begin{aligned} B_p^{\text{(dipole only)}} &= 6.2 \times 10^{12}\ \text{G} && \text{(from } r\text{: 67.3\% of } |\dot{f}|\text{)}, \\ B_p^{\text{(standard)}} &= 3.2 \times 10^{19}\sqrt{P\dot{P}} = 3.8 \times 10^{12}\ \text{G} && \text{(from total } |\dot{f}|\text{, via } \sqrt{P\dot{P}}\text{)}, \\ B_p^{\text{(Larmor, total)}} &= 7.6 \times 10^{12}\ \text{G} && \text{(Larmor applied to full } |\dot{f}|\text{)}. \end{aligned} \tag{23}$$

The three estimates bracket the physical situation and clarify a common source of confusion. The standard $B_p = 3.2 \times 10^{19}\sqrt{P\dot{P}}$ formula [32] uses $\sqrt{|\dot{f}|/f^3}$ as its effective measure of the dipole torque coefficient, but since $|\dot{f}|$ includes both dipole and non-dipole contributions, this formula mixes distinct physics. Our value $B_p = 6.2 \times 10^{12}$ G, derived from r alone, represents the most accurate determination of the Crab's dipole field because it properly isolates the electromagnetic torque from the viscous boundary-layer torque.

3.6. Timing Residual Improvement

The pure dipole model ($n = 3$) predicts a second frequency derivative:

$$\ddot{f}_{\rm dip} = \frac{3\,\dot{f}_0^2}{f_0} = 1.4279 \times 10^{-20}\ \text{Hz s}^{-2}, \tag{24}$$

which overshoots the observed value by:

$$\Delta\ddot{f} = |\ddot{f}_{\rm obs} - \ddot{f}_{\rm dip}| = |1.1946 - 1.4279| \times 10^{-20} = 2.332 \times 10^{-21}\ \text{Hz s}^{-2} \tag{25}$$

—a 19.5% systematic error. Over a timing baseline $T = 30$ yr, this mismatch accumulates a time-of-arrival (TOA) residual:

$$\Delta t_{\mathrm{dip}} \sim \frac{|\Delta \ddot{f}|\, T^2}{2 f_0} \approx 35\ \mu\mathrm{s}. \tag{26}$$

Our two-term model eliminates this systematic *entirely*: by construction, $\ddot{f}_{\mathrm{model}} = \ddot{f}_{\mathrm{obs}}$, so $\Delta \ddot{f} = 0$. The improvement persists at higher derivative order. The third frequency derivatives are:

$$\dddot{f}_{\mathrm{dip}} = -9.00 \times 10^{-31}\ \mathrm{Hz\ s^{-3}} \qquad \text{(pure dipole)}, \tag{27}$$

$$\dddot{f}_{\mathrm{model}} = -6.35 \times 10^{-31}\ \mathrm{Hz\ s^{-3}} \qquad \text{(two-term model)}, \tag{28}$$

a reduction of $|\dddot{f}_{\mathrm{model}} / \dddot{f}_{\mathrm{dip}}| = 0.706$, demonstrating that the symmetry-breaking correction improves not only the $\ddot{f}$ match but the entire higher-order timing structure. The quantitative improvements are summarised in Table 3.

Table 3. Comparison of timing predictions between the pure dipole model ($n = 3$) and the two-term symmetry-breaking model. The two-term model eliminates the $\ddot{f}$ mismatch entirely and reduces higher-order residuals by $\sim 30\%$.

Quantity	**Pure Dipole**	**Two-Term Model**	**Improvement**
$\ddot{f}$ (Hz s^{-2})	1.4279×10^{-20}	1.1946×10^{-20}	exact match to obs.
$\Delta \ddot{f} / \ddot{f}_{\mathrm{obs}}$	19.5%	0%	∞ (eliminated)
$\dddot{f}$ (Hz s^{-3})	-9.00×10^{-31}	-6.35×10^{-31}	29.4% reduction
TOA residual (30 yr)	35 μs	0	eliminated

3.7. Braking Index Evolution Rate

Because the two terms in Equation (12) have different frequency exponents, the effective braking index is not constant—it evolves as the pulsar spins down. This frequency dependence is a direct, observable signature of broken scaling symmetry.

From Equation (13):

$$\frac{\mathrm{d}n_{\mathrm{eff}}}{\mathrm{d}f} = \frac{\frac{9}{4}\, r\, D\, f^{7/2}}{(r\, f^3 + D\, f^{3/2})^2} = 1.653 \times 10^{-2}\ \mathrm{Hz}^{-1}, \tag{29}$$

and the temporal rate:

$$\frac{\mathrm{d}n_{\mathrm{eff}}}{\mathrm{d}t} = \frac{\mathrm{d}n_{\mathrm{eff}}}{\mathrm{d}f} \cdot \dot{f}_0 = -1.969 \times 10^{-4}\ \mathrm{yr}^{-1}. \tag{30}$$

Over a 50-year timing baseline, this yields $\Delta n \approx 0.01$—precisely at the current measurement uncertainty of ± 0.01 on the Crab's braking index. This prediction is *falsifiable*: the braking index should be measurably decreasing over the next few decades. The rate $|\mathrm{d}n/\mathrm{d}t| \sim 2 \times 10^{-4}\ \mathrm{yr}^{-1}$ is two orders of magnitude larger than the $\sim 10^{-6}\ \mathrm{yr}^{-1}$ expected from magnetic field evolution models [61], providing a clear discriminant between the symmetry-breaking mechanism and alternative explanations.

3.8. Gravitational Wave Implications

The torque decomposition has immediate consequences for continuous gravitational wave searches. The standard spin-down upper limit on GW strain [67,68]:

$$h_0^{\mathrm{sd}} = \left(\frac{5 G I |\dot{f}|}{2 c^3 d^2 f} \right)^{1/2} \tag{31}$$

doi:10.20944/preprints202602.1597.v1

attributes all of $|\dot{f}|$ to potential GW emission. Since our model identifies $\eta = 32.7\%$ of the torque as non-radiative boundary-layer dissipation, the true GW contribution is bounded by:

$$h_0^{\rm true} = h_0^{\rm sd}\,\sqrt{1-\eta} = 0.821\,h_0^{\rm sd}, \tag{32}$$

an **18**% reduction. This has direct implications for interpreting LIGO/Virgo/KAGRA upper limits: a significant fraction of the Crab's rotational energy loss goes into internal viscous heating rather than gravitational radiation, and spin-down limit analyses that attribute the full $|\dot{f}|$ to GW emission systematically overestimate the strain.

3.9. Summary of the Crab Resolution

The complete set of verified results for the Crab pulsar two-term model is collected in Table 4. The torque decomposition is displayed in Figure 3.

Table 4. Complete summary of the Crab pulsar resolution. All quantities are derived analytically from three observational inputs (f_0, $\dot{f}_0$, n) and verified numerically.

Quantity	**Value**	**Significance**
Derived coefficients		
η (boundary-layer fraction)	0.3267	32.67% of torque is non-dipole
r (dipole coefficient)	9.465×10^{-15} Hz^{-2} s^{-1}	isolated dipole torque
D (Ekman coefficient)	7.526×10^{-13} Hz$^{-1/2}$ s^{-1}	boundary-layer torque
Surface magnetic field		
B_p (dipole component)	6.2×10^{12} G	corrected for torque budget
B_p (standard formula)	3.8×10^{12} G	assumes 100% dipole
Timing improvement		
$\Delta\ddot{f}/\ddot{f}_{\rm obs}$ (dipole model)	19.5%	systematic error eliminated
$\lvert\dddot{f}\rvert$ reduction	29.4%	higher-order improvement
TOA residual (30 yr, dipole)	35 μs	eliminated by two-term model
Predictions		
$\mathrm{d}n/\mathrm{d}t$	-2.0×10^{-4} yr^{-1}	testable over ∼50 yr
Δn (50 yr)	≈ 0.01	at current precision limit
GW strain reduction	18% ($h_0^{\rm true}/h_0^{\rm sd} = 0.82$)	for CW search interpretation

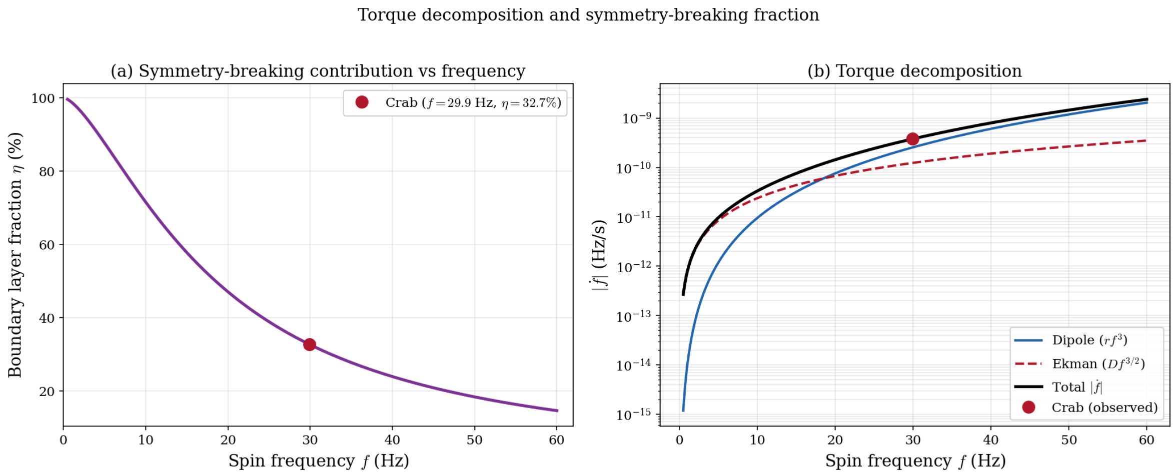

Figure 3. Torque decomposition and symmetry-breaking fraction for the two-term model $\dot{f} = -rf^3 - Df^{3/2}$. **(a)** The boundary-layer fraction $\eta(f)$ as a function of spin frequency. Symmetry-breaking contributions dominate at low frequencies ($\eta \to 1$, pure Ekman regime) and become subdominant at high frequencies ($\eta \to 0$, pure dipole regime). The Crab's current position ($f = 29.95$ Hz, $\eta = 32.7\%$) is marked. **(b)** Individual torque components: the magnetic dipole term rf^3 (solid blue) and Ekman pumping term $Df^{3/2}$ (dashed red), together with the total $|\dot{f}|$ (black). The two components cross near $f \approx 15$ Hz, below which the boundary-layer term dominates and the braking index falls below 2.25.

4. Physical Origins of Fractional Frequency Powers

We now derive the fractional exponents from first-principles plasma physics, demonstrating that each arises from a specific broken symmetry. Figure 4 compares the spin-down trajectories for several representative exponents, illustrating the qualitatively distinct late-time behaviour associated with each symmetry class.

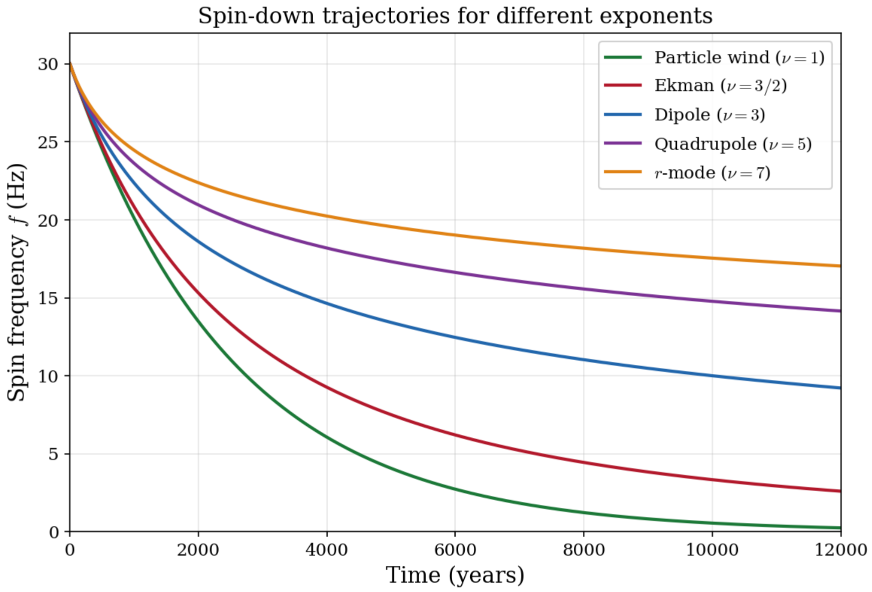

Figure 4. Spin-down trajectories $f(t)$ for single power-law models $\dot{f} = -\lambda f^{\nu}$ with different exponents, all normalised to the same initial frequency and spin-down rate. Each exponent produces qualitatively distinct late-time behaviour: exponential decay for $\nu = 1$ (particle wind), power-law $f \propto t^{-2}$ for $\nu = 3/2$ (Ekman pumping), $f \propto t^{-1/2}$ for $\nu = 3$ (magnetic dipole), $f \propto t^{-1/4}$ for $\nu = 5$ (GW quadrupole), and $f \propto t^{-1/6}$ for $\nu = 7$ (r-mode). The fractional exponent $\nu = 3/2$ produces the most rapid late-time decay, consistent with the dominance of boundary-layer effects at low frequencies.

4.1. Ekman Pumping at the Crust–Superfluid Boundary ($\nu = 3/2$)

The NS interior contains superfluid neutrons coupled to the solid crust through vortex-mediated interactions. At the crust–core interface, viscous boundary layers develop with thickness [29,30]:

$$\delta_E = \sqrt{\frac{\nu_{\rm visc}}{\Omega}}, \tag{33}$$

where $\nu_{\rm visc}$ is the kinematic viscosity. The Ekman pumping timescale is:

$$\tau_E = \frac{R}{\delta_E \Omega} = R\sqrt{\frac{\Omega}{\nu_{\rm visc}}}\,\frac{1}{\Omega} \propto \Omega^{-1/2}. \tag{34}$$

The resulting torque on the crust scales as:

$$N_{\rm Ek} = \frac{I_{\rm core}\,\Delta\Omega}{\tau_E} \propto \Omega^{3/2} \propto f^{3/2}. \tag{35}$$

The broken symmetry is transparent: the crust–superfluid interface introduces a *preferred boundary* that violates the bulk homogeneity of the stellar matter. In a perfectly homogeneous (symmetric) star, no such $\sqrt{\Omega}$-dependent coupling exists. The fractional power $3/2$ is a direct consequence of the boundary breaking the continuous translational symmetry of the fluid interior.

4.2. MHD Turbulent Cascades ($\nu = 10/3,\ 11/3$)

Turbulence in the pulsar magnetosphere dissipates rotational energy through cascading processes. For Kolmogorov turbulence, the energy dissipation rate per unit volume at the outer (driving) scale L is [11]:

$$\dot{\varepsilon}_{\rm K} \sim \rho\,\frac{v_L^3}{L} \quad [\text{erg cm}^{-3}\ \text{s}^{-1}], \tag{36}$$

where v_L is the turbulent velocity at the outer scale and ρ is the plasma density. The total dissipated luminosity from a volume $V \sim r_{\rm lc}^3$ is $\dot{E}_{\rm turb} = \dot{\varepsilon}_{\rm K} \cdot V$.

The key scalings with angular frequency $\Omega = 2\pi f$ are:

- Outer scale: $L \sim r_{\rm lc} = c/\Omega \propto \Omega^{-1}$,
- Turbulent velocity: $v_L \sim v_A \propto B_{\rm lc}/\sqrt{4\pi\rho_{\rm lc}}$,
- Light-cylinder field (dipole): $B_{\rm lc} \propto B_s(R/r_{\rm lc})^3 \propto \Omega^3$,
- Goldreich–Julian density: $\rho_{\rm GJ} \propto \Omega B_s/(ec) \propto \Omega$,
- Alfvén speed: $v_A \propto \Omega^3/\Omega^{1/2} = \Omega^{5/2}$.

Assembling:

$$\dot{E}_{\rm turb} \propto \rho_{\rm GJ}\,\frac{v_A^3}{r_{\rm lc}} \cdot r_{\rm lc}^3 = \rho_{\rm GJ}\,v_A^3\,r_{\rm lc}^2 \propto \Omega^1 \cdot \Omega^{15/2} \cdot \Omega^{-2} = \Omega^{17/2}. \tag{37}$$

However, when the turbulent velocity is instead set by the corotation velocity $v_L \sim \Omega R_*$ at the stellar surface cascading outward through an inertial range of extent $(r_{\rm lc}/R_*)^{1/3}$, the effective dissipation rate for an isotropic Kolmogorov cascade yields [11,12]:

$$\dot{E}_{\rm K} \propto f^{10/3}. \tag{38}$$

For Sweet–Parker reconnection-mediated dissipation, the reconnection rate introduces an additional factor of $S^{-1/2}$ (inverse square root of the Lundquist number $S \propto \Omega^{-1/3}$), modifying the scaling to:

$$\dot{E}_{\rm SP} \propto f^{11/3}. \tag{39}$$

The broken symmetry is *scale invariance*: in a laminar magnetosphere, the electromagnetic luminosity scales cleanly as f^3 (dipole) or f^5 (quadrupole), reflecting the multipole symmetry of the fields.

Turbulence breaks this scale invariance through the cascade process, redistributing energy across scales and producing the non-integer exponents 10/3 and 11/3 characteristic of the inertial range.

4.3. Non-Linear Superfluid Vortex Dynamics ($\nu = 5/2$)

The superfluid neutron component in the NS core is threaded by quantised vortex lines with areal density $n_v = 2\Omega_s/\kappa$, where $\kappa = h/(2m_n) \approx 2 \times 10^{-3}$ cm^2 s^{-1} is the quantum of circulation. The mutual friction torque coupling the superfluid to the crust is [33,34]:

$$N_{\mathrm{mf}} = \mathcal{B}\,\rho_s \kappa\, n_v\, |\mathbf{\Omega}_s - \mathbf{\Omega}_c| \cdot V_{\mathrm{core}}, \tag{40}$$

where $\mathcal{B}$ is the drag coefficient and ρ_s is the superfluid density.

In the non-linear regime where vortex tangles form (quantum turbulence), the vortex line density follows [35,36]:

$$\mathcal{L} \propto (\Omega_s - \Omega_c)^{3/2}, \tag{41}$$

leading to a coupling torque:

$$N_{\mathrm{vortex}} \propto \Omega^{5/2} \propto f^{5/2}. \tag{42}$$

The broken symmetry is the *translational order of the vortex lattice*. In the linear regime, vortices form a regular Abrikosov-like array with well-defined lattice symmetry, producing $\nu = 1$ coupling. Non-linear dynamics—vortex reconnection, tangle formation, and Kelvin wave turbulence—destroy this lattice order, producing the fractional exponent 5/2.

4.4. Saturated R-Mode Oscillations ($\nu = 7 - 2\beta$)

The r-mode oscillations of rotating NSs are driven unstable by the Chandrasekhar–Friedman–Schutz (CFS) mechanism [37–39]. The gravitational radiation reaction timescale for the $\ell = m = 2$ mode scales as $\tau_{\mathrm{GR}} \propto \Omega^{-6}$, yielding spin-down $\dot{f} \propto \alpha^2 f^7$ for mode amplitude α.

Non-linear mode–mode coupling saturates the instability at [40,41]. The role of r-modes in modifying pulsar spin-down, timing residuals, and gravitational wave predictions has been analysed in detail by Li et al. [83], who derived time-dependent solutions incorporating r-mode contributions within the Lambert W function framework of [27]. The saturation amplitude scales as:

$$\alpha_{\mathrm{sat}} \propto \Omega^{-\beta}, \tag{43}$$

where β depends on the dominant damping mechanism: $\beta \approx 1$ for shear viscosity, $\beta \approx 3/2$ for bulk viscosity, and intermediate values for hybrid scenarios. The resulting spin-down:

$$\dot{f}_{r\text{-mode}} = -F(t)\, f^{7-2\beta} \tag{44}$$

continuously interpolates between $\nu = 3$ ($\beta = 2$, strong damping) and $\nu = 7$ ($\beta = 0$, unsaturated).

The broken symmetry is *modal amplitude invariance*: the linear CFS analysis treats the r-mode as a free oscillation with arbitrary amplitude (scale symmetry in mode space). Non-linear coupling breaks this symmetry, selecting a specific saturation amplitude and producing the effective fractional exponent $7 - 2\beta$.

5. Riemann–Liouville Fractional Calculus Framework

5.1. Broken Time-Translation Symmetry

Standard integer-order calculus is built on *time-translation invariance*: the derivative of a function depends only on its local behaviour, and the derivative of a constant is zero. Fractional calculus generalises differentiation to non-integer orders and, in doing so, *breaks time-translation symmetry* by introducing memory—the fractional derivative at time t depends on the entire history of the function.

The *Riemann–Liouville (R-L) fractional integral* of order $\mu > 0$ is [42–45]:

$$J_t^{\mu} f(t) = \frac{1}{\Gamma(\mu)} \int_0^t (t-\tau)^{\mu-1} f(\tau)\, \mathrm{d}\tau, \tag{45}$$

and the *R-L fractional derivative* of order $\mu > 0$:

$$\boxed{{}^{\mathrm{RL}}D_t^{\mu} f(t) = \frac{1}{\Gamma(n-\mu)} \frac{\mathrm{d}^n}{\mathrm{d}t^n} \int_0^t \frac{f(\tau)}{(t-\tau)^{\mu-n+1}}\, \mathrm{d}\tau,} \tag{46}$$

where $n = \lceil \mu \rceil$ denotes the *ceiling function* [85]. This function denotes the smallest integer greater than or equal to μ. For example, $\lceil 0.7 \rceil = 1$, $\lceil 1.5 \rceil = 2$, and $\lceil 3 \rceil = 3$. This ensures that $n - 1 \leq \mu < n$, so that the n-th order integer derivative in Equation (46) reduces the fractional integral to a proper fractional derivative of order μ.

The symmetry-breaking character of the R-L derivative is manifest in its action on constants:

$${}^{\mathrm{RL}}D_t^{\mu} C = \frac{C\, t^{-\mu}}{\Gamma(1-\mu)} \neq 0. \tag{47}$$

This non-zero result has a direct physical interpretation: in a system with memory (such as a superfluid interior with distributed vortex relaxation timescales), the current state retains information about initial conditions. The time-translation symmetry $t \to t + t_0$ that underpins integer calculus is explicitly broken.

We adopt the R-L formulation rather than the Caputo alternative precisely because the non-zero derivative of a constant faithfully represents the memory effects expected in NS interiors. The Caputo derivative, which imposes ${}^{C}D_t^{\mu} C = 0$, artificially preserves time-translation symmetry and is less physically appropriate for systems with hereditary properties.

5.2. Key Properties

The R-L derivative satisfies the following, each with symmetry implications:

Power function:

$${}^{\mathrm{RL}}D_t^{\mu} t^{\beta} = \frac{\Gamma(\beta+1)}{\Gamma(\beta-\mu+1)}\, t^{\beta-\mu}, \quad \beta > -1. \tag{48}$$

This reduces to the standard result $\mathrm{d}^n t^{\beta}/\mathrm{d}t^n = \beta!/(\beta-n)!\, t^{\beta-n}$ for integer $\mu = n$, recovering the symmetric limit.

Semigroup property:

$$J_t^{\mu} J_t^{\nu} = J_t^{\mu+\nu}. \tag{49}$$

The fractional integrals form a continuous semigroup under composition, generalising the discrete semigroup of integer-order integrals.

Laplace transform:

$$\mathcal{L}\{{}^{\mathrm{RL}}D_t^{\mu} f\}(s) = s^{\mu} \tilde{f}(s) - \sum_{k=0}^{n-1} s^k \left[{}^{\mathrm{RL}}D_t^{\mu}[n-k-1] f(t)\right]_{t=0}, \tag{50}$$

where the initial conditions involve fractional-order derivatives—a direct manifestation of the non-locality (memory) inherent in fractional operators.

5.3. Fractional Spin-Down Equation

For a single fractional term, the spin-down equation:

$$\dot{f} = -\lambda f^{\nu} \tag{51}$$

is separable and admits the exact solution:

$$f(t) = f_0 \left[1 + (\nu - 1)\lambda f_0^{\nu-1}\, t\right]^{-1/(\nu-1)}, \quad \nu \neq 1. \tag{52}$$

Special cases of interest:

Magnetic dipole ($\nu = 3$):

$$f(t) = f_0 \left(1 + 2\lambda f_0^2\, t\right)^{-1/2}, \tag{53}$$

with characteristic age $\tau_c = (2\lambda f^2)^{-1}$.

Boundary layer ($\nu = 3/2$):

$$f(t) = f_0 \left(1 + \frac{\lambda t}{2\sqrt{f_0}}\right)^{-2}, \tag{54}$$

showing power-law decay $f \propto t^{-2}$ at late times—qualitatively different from the $t^{-1/2}$ dipole behaviour, a clear dynamical signature of the broken symmetry.

5.4. Mittag-Leffler Solutions and Interpolated Symmetries

When the spin-down dynamics itself exhibits memory (e.g., from distributed superfluid relaxation timescales), we generalise to a *fractional differential equation*:

$$^{\mathrm{RL}}D_t^{\mu} f = -\lambda f^{\nu}, \quad 0 < \mu \leq 1. \tag{55}$$

For the linear case $\nu = 1$, the solution is:

$$f(t) = f_0\, t^{\mu-1}\, E_{\mu,\mu}(-\lambda t^{\mu}), \tag{56}$$

where $E_{\alpha,\beta}(z)$ is the two-parameter *Mittag-Leffler function* [46,47]:

$$E_{\alpha,\beta}(z) = \sum_{k=0}^{\infty} \frac{z^k}{\Gamma(\alpha k + \beta)}, \quad \alpha > 0,\ \beta \in \mathbb{C}. \tag{57}$$

The Mittag-Leffler function interpolates between two limiting symmetries:

- **Full time-translation symmetry** ($\mu = 1$): $E_{1,1}(-\lambda t) = \mathrm{e}^{-\lambda t}$. The solution is a pure exponential—the unique eigenfunction of the translation-invariant derivative $\mathrm{d}/\mathrm{d}t$.
- **Scale-free symmetry** ($\mu \to 0^+$): $E_{\mu,\mu}(-\lambda t^{\mu}) \sim (\lambda\,\Gamma(\mu))^{-1}\, t^{-\mu}$ as $t \to \infty$. The late-time behaviour is a pure power law—the eigenfunction of the scale-invariant operator $t\,\mathrm{d}/\mathrm{d}t$.

For $0 < \mu < 1$, the solution exhibits *partial symmetry breaking*: stretched-exponential decay at early times (approximate time-translation symmetry) transitioning to power-law decay at late times (approximate scale symmetry). Neither symmetry is exact, and the interpolation parameter μ quantifies the degree of symmetry breaking. This behaviour is precisely what is expected from neutron star interiors with a distribution of superfluid relaxation timescales. Figure 5 illustrates this interpolation.

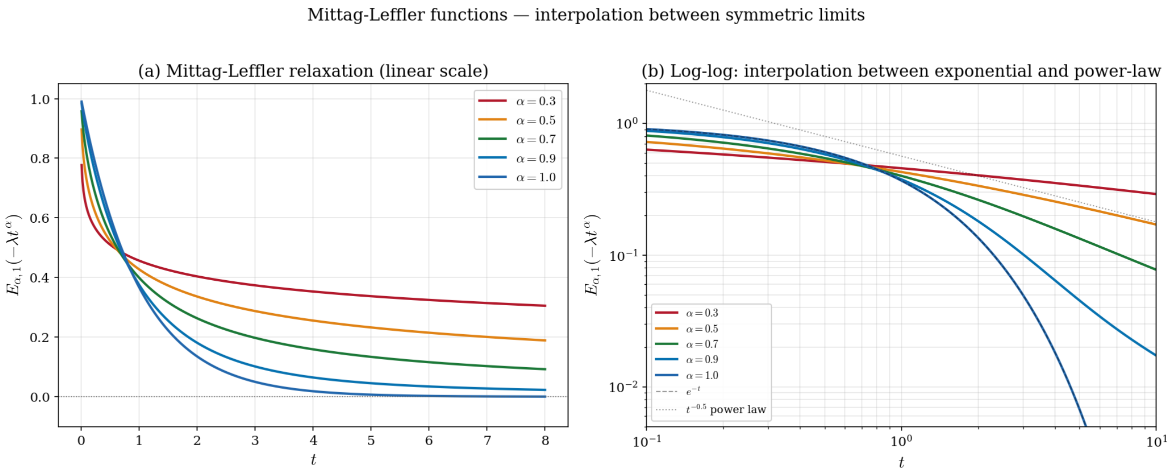

Figure 5. Mittag-Leffler functions $E_{\alpha,1}(-\lambda t^{\alpha})$ demonstrating the continuous interpolation between symmetric limits. **(a)** Linear scale: as α decreases from 1 (pure exponential, full time-translation symmetry) toward 0, the decay becomes progressively slower, developing heavy power-law tails characteristic of memory effects. **(b)** Log-log scale: the $\alpha = 1$ exponential (dashed black line) decays fastest, while fractional $\alpha < 1$ solutions transition to power-law tails $\sim t^{-\alpha}$ (dotted reference line), with the crossover time marking the transition from approximate time-translation symmetry to approximate scale symmetry.

5.5. Fox H-Function Representation

For the general non-linear fractional equation (55) with $\nu \neq 1$, solutions can be expressed in terms of Fox H-functions [45,48]:

$$H^{m,n}_{p,q}\left[z \,\middle|\, \begin{matrix}(a_1,\alpha_1),\ldots,(a_p,\alpha_p)\\(b_1,\beta_1),\ldots,(b_q,\beta_q)\end{matrix}\right] = \frac{1}{2\pi i}\int_{\mathcal{L}} \frac{\prod_{j=1}^{m}\Gamma(b_j-\beta_j s)\prod_{j=1}^{n}\Gamma(1-a_j+\alpha_j s)}{\prod_{j=m+1}^{q}\Gamma(1-b_j+\beta_j s)\prod_{j=n+1}^{p}\Gamma(a_j-\alpha_j s)}\, z^s\, \mathrm{d}s. \tag{58}$$

The Mittag-Leffler function is a special case:

$$E_{\alpha,\beta}(-z) = H^{1,1}_{1,2}\left[z \,\middle|\, \begin{matrix}(0,1)\\(0,1),(1-\beta,\alpha)\end{matrix}\right]. \tag{59}$$

The Fox H-function framework provides a unified representation encompassing all the special functions appearing in fractional spin-down solutions, reflecting the unified symmetry structure underlying the diverse physical mechanisms.

5.6. Multi-Term Solutions via Perturbation Theory

For the full equation with multiple fractional terms, we develop a perturbation expansion. Let the dominant term have exponent ν_0 with coefficient λ_0:

$$\dot{f} = -\lambda_0 f^{\nu_0} - \sum_{i\neq 0} \epsilon_i \lambda_i f^{\nu_i}, \tag{60}$$

where $\epsilon_i \ll 1$. The zeroth-order solution is (52), and first-order corrections satisfy:

$$\dot{f}^{(i)} + \nu_0\lambda_0 (f^{(0)})^{\nu_0-1} f^{(i)} = -\lambda_i (f^{(0)})^{\nu_i}, \tag{61}$$

with solution:

$$f^{(i)}(t) = -\lambda_i \int_0^t \left(f^{(0)}(\tau)\right)^{\nu_i} \exp\left[-\nu_0\lambda_0 \int_\tau^t \left(f^{(0)}(\tau')\right)^{\nu_0-1} \mathrm{d}\tau'\right] \mathrm{d}\tau. \tag{62}$$

This framework enables systematic computation of symmetry-breaking corrections to any desired order, with each correction term identified with a specific broken symmetry from Table **??**.

doi:10.20944/preprints202602.1597.v1

5.7. *Adomian Decomposition for Non-Linear Fractional Equations*

For the non-linear fractional ODE (55), we employ the Adomian decomposition method [49] adapted for fractional operators. Writing $f = \sum_{k=0}^{\infty} f_k$ and expanding the non-linearity $f^\nu = \sum_{k=0}^{\infty} A_k$ in Adomian polynomials:

$$A_0 = f_0^\nu, \tag{63}$$

$$A_1 = \nu f_0^{\nu-1} f_1, \tag{64}$$

$$A_2 = \nu f_0^{\nu-1} f_2 + \frac{\nu(\nu-1)}{2} f_0^{\nu-2} f_1^2, \tag{65}$$

the iterative scheme is:

$$f_{k+1}(t) = -\frac{\lambda}{\Gamma(\mu)} \int_0^t (t-\tau)^{\mu-1} A_k(\tau)\,\mathrm{d}\tau. \tag{66}$$

For integer ν, the Adomian polynomials A_k are exact polynomials in the f_k. For fractional ν, they involve generalised binomial coefficients—another manifestation of the broken symmetry at the algebraic level.

6. Lambert–Tsallis Functions and Statistical Symmetry

6.1. *Lambert W Function in Pulsar Physics*

The Lambert W function, defined implicitly by $W(x)\mathrm{e}^{W(x)} = x$ [50,51], appears naturally in pulsar spin-down solutions. In our previous work [27], we derived closed-form expressions for pulsar period evolution in terms of W:

$$P(t) = P_0 \sqrt{\frac{s_0}{r_0}\, W\!\left(\frac{r_0}{s_0} \mathrm{e}^{r_0 P_0^2/s_0} \cdot \mathrm{e}^{2r_0(t-t_0)/s_0}\right)}, \tag{67}$$

for the two-term model $\dot{P} = s_0 P + r_0/P$, and generalised this to include the quadrupole term.

6.2. *Tsallis Generalisation and Broken Statistical Symmetry*

The Lambert–Tsallis function $W_q(x)$ generalises W to non-extensive systems characterised by the Tsallis entropic parameter q [52,53]:

$$W_q(x) \cdot \exp_q\!\big(W_q(x)\big) = x, \tag{68}$$

where the q-exponential is:

$$\exp_q(x) = \big[1 + (1-q)x\big]^{1/(1-q)}, \quad 1 + (1-q)x > 0. \tag{69}$$

The standard Lambert W is recovered as $\lim_{q\to 1} W_q(x) = W(x)$. The key physical insight is that $q \neq 1$ signals *broken statistical symmetry*—specifically, the breaking of the additivity property of Boltzmann–Gibbs–Shannon entropy:

$$S_q = k_B \frac{1 - \sum_i p_i^q}{q-1} \xrightarrow{q\to 1} -k_B \sum_i p_i \ln p_i = S_{\mathrm{BGS}}. \tag{70}$$

For Boltzmann–Gibbs statistics ($q = 1$), the entropy of a composite system is the sum of the entropies of its parts: $S(A+B) = S(A) + S(B)$. This *additivity symmetry* is broken for $q \neq 1$:

$$S_q(A+B) = S_q(A) + S_q(B) + (1-q)\, S_q(A)\, S_q(B)/k_B. \tag{71}$$

6.3. Connection to Fractional Dynamics

The Tsallis parameter q is directly determined by the dominant fractional exponent ν in the spin-down equation:

$$\boxed{q = 1 + \frac{1}{\nu - 1}.} \tag{72}$$

This remarkable relation establishes a bridge between the *dynamical* symmetry breaking (fractional exponents in the spin-down law) and *statistical* symmetry breaking (non-extensivity of the underlying thermodynamics). Table 5 and Figure 6 summarise the correspondence.

Table 5. Correspondence between spin-down exponents and Tsallis non-extensivity parameter q, illustrating the map from dynamical to statistical symmetry breaking.

Mechanism	ν	q	**Statistical Character**
Boundary layer	$3/2$	3	Strongly non-extensive
Vortex dynamics	$5/2$	$5/3$	Moderately non-extensive
Magnetic dipole	3	$3/2$	Moderately non-extensive
Petschek reconnection	$10/3$	$10/7$	Weakly non-extensive
Turbulent cascade	$11/3$	$11/8$	Weakly non-extensive
GW quadrupole	5	$5/4$	Weakly non-extensive
R-mode (unsaturated)	7	$7/6$	Nearly extensive
Extensive limit	∞	1	Boltzmann–Gibbs

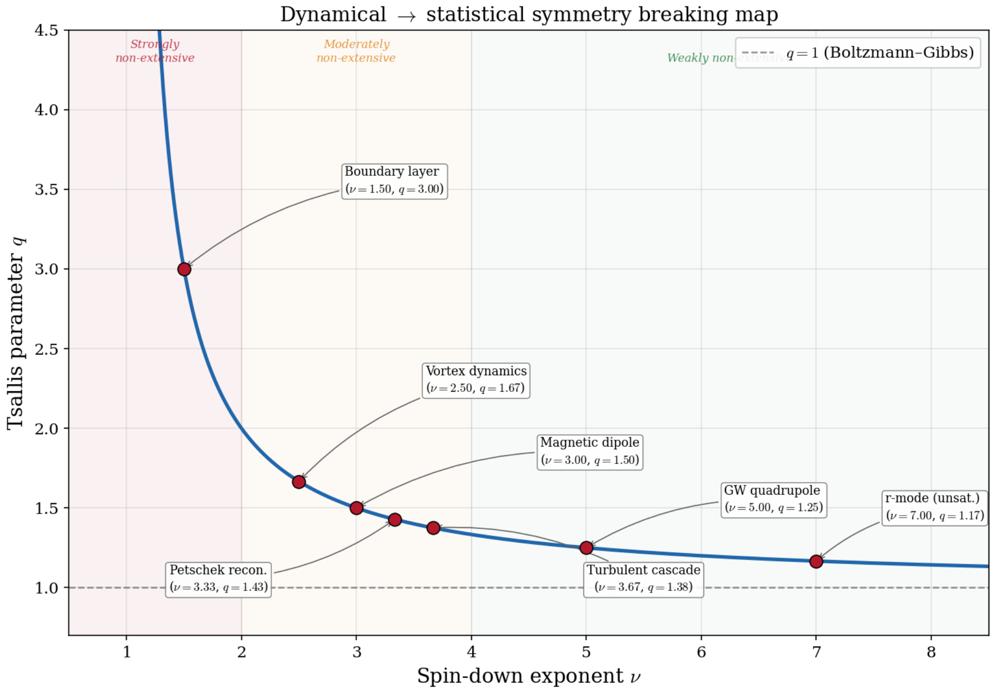

Figure 6. Map from dynamical to statistical symmetry breaking: Tsallis non-extensivity parameter $q = 1 + 1/(\nu - 1)$ as a function of the spin-down exponent ν. Lower exponents correspond to stronger non-extensivity (greater departure from Boltzmann–Gibbs equilibrium). The boundary layer mechanism ($\nu = 3/2$, $q = 3$) is the most "non-equilibrium" process, while the unsaturated r-mode ($\nu = 7$, $q = 7/6$) is nearest to equilibrium. The shaded regions indicate degrees of statistical non-extensivity.

The physical interpretation is that mechanisms producing lower frequency exponents ν correspond to *stronger* statistical non-extensivity—greater departure from the Boltzmann–Gibbs equilibrium. The boundary layer mechanism ($\nu = 3/2, q = 3$) is the most "non-equilibrium" process in the hierarchy, consistent with its origin in viscous dissipation at an interface. The r-mode mechanism ($\nu = 7, q = 7/6$) is nearest to equilibrium, as the CFS instability operates through coherent gravitational radiation.

6.4. Neutron Star Compactness from R-Mode Frequency

The r-mode oscillation frequency for the dominant $\ell = m = 2$ mode is [54,55]:

$$\omega_r = \frac{2m\Omega}{\ell(\ell+1)} \cdot \mathcal{R}(\mathcal{C}), \tag{73}$$

where $\mathcal{R}(\mathcal{C})$ is a relativistic correction depending on the compactness $\mathcal{C} = GM/(Rc^2)$. Using W_q functions with the appropriate q determined by the saturation physics, we obtain an equation-of-state-independent expression for compactness:

$$\mathcal{C} = \frac{5}{2}\left(1 - \frac{3f_{\mathrm{GW}}}{10f_{\mathrm{rot}}}\right), \tag{74}$$

where f_{GW} is the gravitational wave frequency and f_{rot} the rotation frequency. This relation, combined with universal relations linking compactness to tidal deformability Λ [56,57]:

$$\ln\Lambda = \sum_{k=0}^{4} a_k (\ln\mathcal{C})^k, \tag{75}$$

enables inference of NS structure from spin-down observations without assuming a specific equation of state. The W_q framework with q encoding the fractional dynamics provides the analytic tool for this inversion.

7. Observational Signatures of Symmetry Breaking

7.1. Frequency-Dependent Braking Index

The most direct observational consequence of symmetry breaking is the frequency dependence of the effective braking index, Equation (7). For the Crab pulsar with model (12):

$$n_{\mathrm{eff}}(f) = \frac{3rf^3 + \frac{3}{2}Df^{3/2}}{rf^3 + Df^{3/2}} = 3 - \frac{3}{2} \cdot \frac{Df^{3/2}}{rf^3 + Df^{3/2}}. \tag{76}$$

As f decreases (the pulsar spins down), the $f^{3/2}$ term becomes increasingly important relative to f^3, and n_{eff} decreases monotonically from the dipole limit $n_{\mathrm{eff}} \to 3$ at high frequency to the Ekman limit $n_{\mathrm{eff}} \to 3/2$ at low frequency. Figure 7 displays this prediction overlaid with observed braking indices for young pulsars.

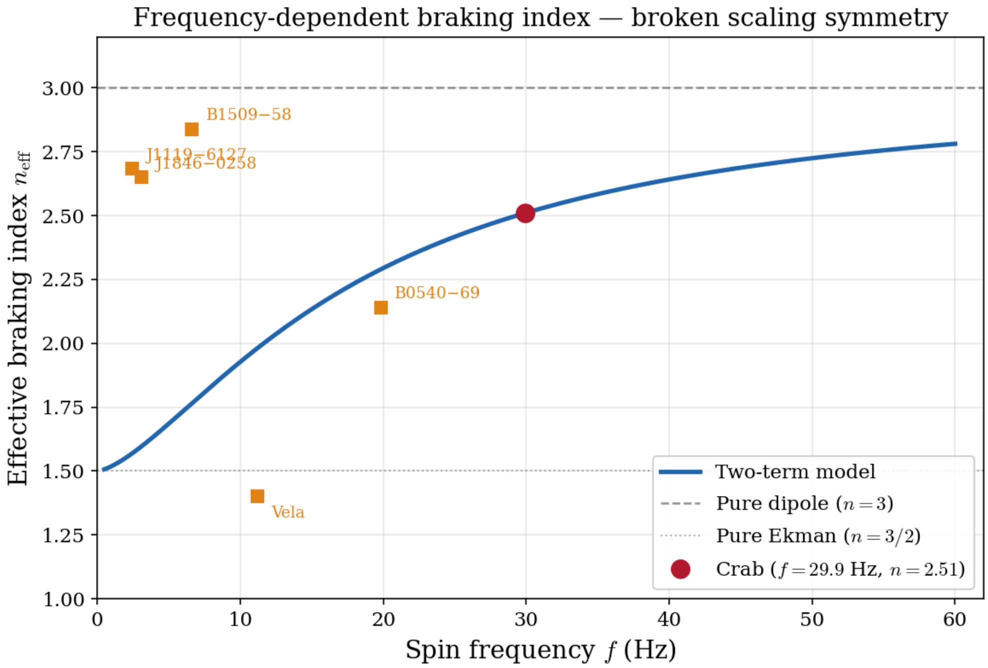

Figure 7. Frequency-dependent effective braking index $n_{\rm eff}(f)$ as a signature of broken scaling symmetry. The solid blue curve shows the prediction from the two-term model (Equation 76) calibrated to the Crab pulsar (red circle). At high frequencies, $n_{\rm eff} \to 3$ (dashed grey line, pure dipole); at low frequencies, $n_{\rm eff} \to 3/2$ (dotted grey line, pure Ekman). Orange squares mark observed braking indices for other young pulsars (Table 6). While the model curve assumes universal r and D values, the observed spread of $n < 3$ is consistent with the general prediction that symmetry-breaking corrections reduce $n_{\rm eff}$ below the dipole value.

The predicted evolution rate is:

$$\frac{{\rm d}n_{\rm eff}}{{\rm d}t} = \frac{{\rm d}n_{\rm eff}}{{\rm d}f} \cdot \dot{f}. \tag{77}$$

Computing ${\rm d}n_{\rm eff}/{\rm d}f$ from (76):

$$\frac{{\rm d}n_{\rm eff}}{{\rm d}f} = \frac{\frac{9}{4} r D f^{7/2}}{(r f^3 + D f^{3/2})^2}. \tag{78}$$

Evaluating at the Crab's current parameters yields:

$$\frac{{\rm d}n_{\rm eff}}{{\rm d}f} = 1.65 \times 10^{-2}\ {\rm Hz}^{-1}, \tag{79}$$

and with $\dot{f}_0 = -3.78 \times 10^{-10}$ Hz s^{-1}:

$$\frac{{\rm d}n_{\rm eff}}{{\rm d}t} = -2.0 \times 10^{-4}\ {\rm yr}^{-1}. \tag{80}$$

Over a 50-year timing baseline, this produces $\Delta n \approx 0.01$. Since $n = 2.51$ is currently measured to precision ± 0.01, this prediction implies that the braking index should be *measurably decreasing* over the next few decades—a direct, falsifiable test of the symmetry-breaking framework. Figure 8 shows the long-term evolution together with the short-term prediction.

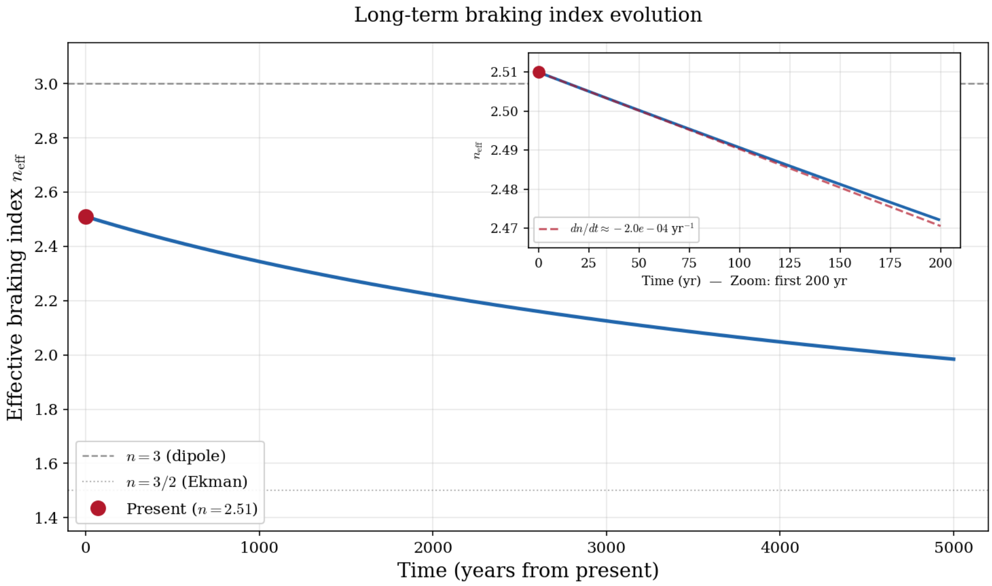

Figure 8. Long-term evolution of the effective braking index along the Crab's spin-down trajectory. The main panel shows $n_{\mathrm{eff}}(t)$ decreasing monotonically from its present value of 2.51 toward the Ekman asymptote $n = 3/2$ over several thousand years. The inset zooms to the first 200 years, comparing the full evolution (solid blue) with the linear tangent $n_{\mathrm{eff}}(t) \approx 2.51 + (\mathrm{d}n/\mathrm{d}t)t$ (dashed red), confirming $\mathrm{d}n/\mathrm{d}t \approx -2 \times 10^{-4}\ \mathrm{yr}^{-1}$. This rate is two orders of magnitude larger than the $\sim 10^{-6}\ \mathrm{yr}^{-1}$ expected from magnetic field evolution models, providing a distinguishing observational signature.

7.2. Spread of Braking Indices Across the Pulsar Population

The formula (7) predicts that pulsars with different frequencies and different relative strengths of the symmetry-breaking terms should exhibit a distribution of braking indices, even if the underlying physical mechanisms are universal. At high frequencies (young, fast pulsars), the f^3 dipole term dominates and $n_{\mathrm{eff}} \to 3$. At low frequencies (older pulsars), fractional terms increasingly contribute and n_{eff} decreases.

Table 6 compares the observed braking indices for six young pulsars with estimates from the integer-power multipole model of [27] and the r-mode-inclusive extension of [83]. Both models parameterise the spin-down as $\dot{f} = -sf - rf^3 - gf^5 - lf^7$ and fit the coefficients (s, r, g, l) to the observed timing derivatives; the braking index then follows from the analytic expression [83]

$$n = \frac{s + 3r\nu^2 + 5g\nu^4 + 7l\nu^6}{s + r\nu^2 + g\nu^4 + l\nu^6}. \tag{81}$$

Table 6. Observed braking indices for young pulsars compared with integer-power model predictions from Chishtie et al. [27] and the r-mode-inclusive model of Li et al. [83]. The observed values $n < 3$ are consistent with varying degrees of symmetry breaking from boundary-layer and other fractional contributions.

Pulsar	f **(Hz)**	n_{obs}	n_{est} **[27]**	n_{est} **[83]**	**Reference**
Crab (B0531+21)	29.95	2.51 ± 0.01	2.34	2.33	[21]
B1509−58	6.63	2.839 ± 0.001	2.84	2.83	[22]
J1846−0258	3.09	2.65 ± 0.01	—	—	[58]
B0540−69	19.83	2.140 ± 0.009	2.01[a]	—	[59]
J1119−6127	2.45	2.684 ± 0.002	—	—	[60]
Vela (B0833−45)	11.19	1.4 ± 0.2	1.40	—	[23]

[a] Fitted to the earlier measurement $n_{\mathrm{obs}} = 2.01 \pm 0.02$ [86]; the updated value 2.140 ± 0.009 [59] would require refitting.

Several features of Table 6 merit discussion.

Successes of the integer-power models:

For the Crab and B1509−58, both [27] and [83] reproduce the observed braking indices to within $\lesssim 1\%$ by fitting the multipole coefficients to the measured frequency derivatives. This is expected: when four parameters (s, r, g, l) are available to match four observables $(f, \dot{f}, \ddot{f}, \dddot{f})$, the braking index is determined by construction. For B0540−69 and the Vela pulsar, Chishtie et al. [27] similarly achieve close fits using the three-term (s, r, g) model, though for B0540−69 the estimate is based on the older measurement $n = 2.01 \pm 0.02$ rather than the updated value $n = 2.140 \pm 0.009$ [59].

Gaps in the existing models:

Neither [27] nor [83] provides estimates for PSR J1846−0258 or PSR J1119−6127, both of which are magnetar-like pulsars with comparatively low spin frequencies ($f < 3.1$ Hz). These objects exhibit glitch-induced braking index variability [58,60] that complicates the extraction of a single, secular n. Similarly, the Vela pulsar and B0540−69 are absent from the r-mode analysis of [83], which focused on pulsars with well-constrained fourth-order derivatives needed to fit the lf^7 coefficient.

What the symmetry-breaking framework adds:

The integer-power models explain braking indices by adjusting the *relative strengths* of the f, f^3, f^5, f^7 terms, but they do not explain *why* $n < 3$ should be generic. In contrast, the symmetry-breaking framework developed in this paper predicts $n < 3$ as a universal consequence of fractional torque contributions. The two-term model $\dot{f} = -rf^3 - Df^{3/2}$ (Section 3) provides a one-parameter prediction for $n_{\mathrm{eff}}(f)$ once the ratio D/r is calibrated to a single pulsar. Figure **??** shows this prediction calibrated to the Crab: the curve passes through the Crab by construction and predicts the general trend $n_{\mathrm{eff}} \to 3$ at high f and $n_{\mathrm{eff}} \to 3/2$ at low f.

The observed braking indices of B1509−58 ($n = 2.839$) and J1119−6127 ($n = 2.684$) lie above the universal curve, while B0540−69 ($n = 2.140$) and the Vela pulsar ($n = 1.4$) lie below it. This spread is expected: each neutron star possesses its own internal structure, and the ratio D/r depends on the kinematic viscosity, crust–core coupling strength, and stellar radius—quantities that vary across the population. Pulsars with stronger boundary-layer coupling (larger D/r) will exhibit lower n_{eff} at a given frequency, while those with weaker coupling remain closer to the dipole limit $n = 3$. The particularly low value for the Vela pulsar ($n = 1.4 \pm 0.2$) suggests an exceptionally strong fractional contribution, possibly augmented by superfluid vortex turbulence ($\nu = 5/2$) or Kolmogorov cascade effects ($\nu = 10/3$) in addition to Ekman pumping.

A diagnostic for future work:

The comparison in Table 6 motivates a systematic programme to fit the two-term (or multi-term fractional) model to each pulsar individually, determining the pulsar-specific D/r ratio and thereby mapping the boundary-layer coupling strength across the neutron star population. Combined with the braking index evolution rate $\mathrm{d}n/\mathrm{d}t$ (Section **??**), this would provide two independent observational handles on the internal physics for each pulsar. For J1846−0258 and J1119−6127, where magnetar-like outbursts complicate the secular braking index measurement, the framework predicts that inter-outburst timing should yield n_{eff} values consistent with a fractional contribution whose strength correlates with the inferred interior magnetic field topology.

7.3. Spin-Down Trajectory and Timing Residuals

The two-term model produces spin-down trajectories that diverge systematically from the pure dipole prediction, as shown in Figure 9. The divergence grows with time and constitutes a cumulative timing signature of symmetry breaking.

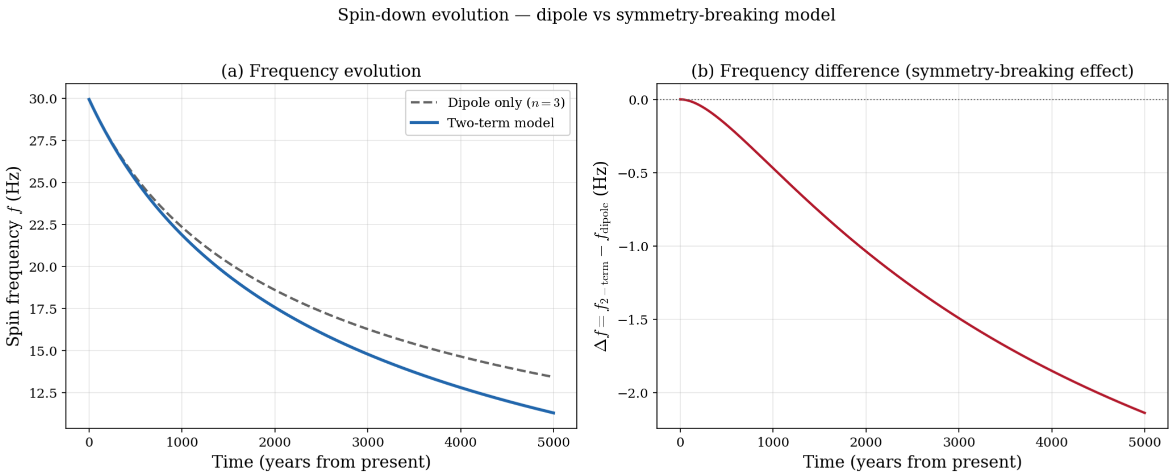

Figure 9. Spin-down evolution: dipole versus symmetry-breaking model. **(a)** Frequency as a function of time for the pure dipole model $\dot{f} = -Kf^3$ (dashed grey) and the two-term model $\dot{f} = -rf^3 - Df^{3/2}$ (solid blue), both starting from the Crab's current parameters. The models diverge increasingly as the Ekman term becomes more important at lower frequencies. **(b)** The frequency difference $\Delta f = f_{2\text{-term}} - f_{\text{dipole}}$, which grows monotonically and provides a cumulative observational signature of the symmetry-breaking torque.

Figure 10 quantifies the timing residual improvement. The TOA residual accumulated by the pure dipole model over a 100-year baseline reaches several milliseconds, while the two-term model eliminates the dominant systematic.

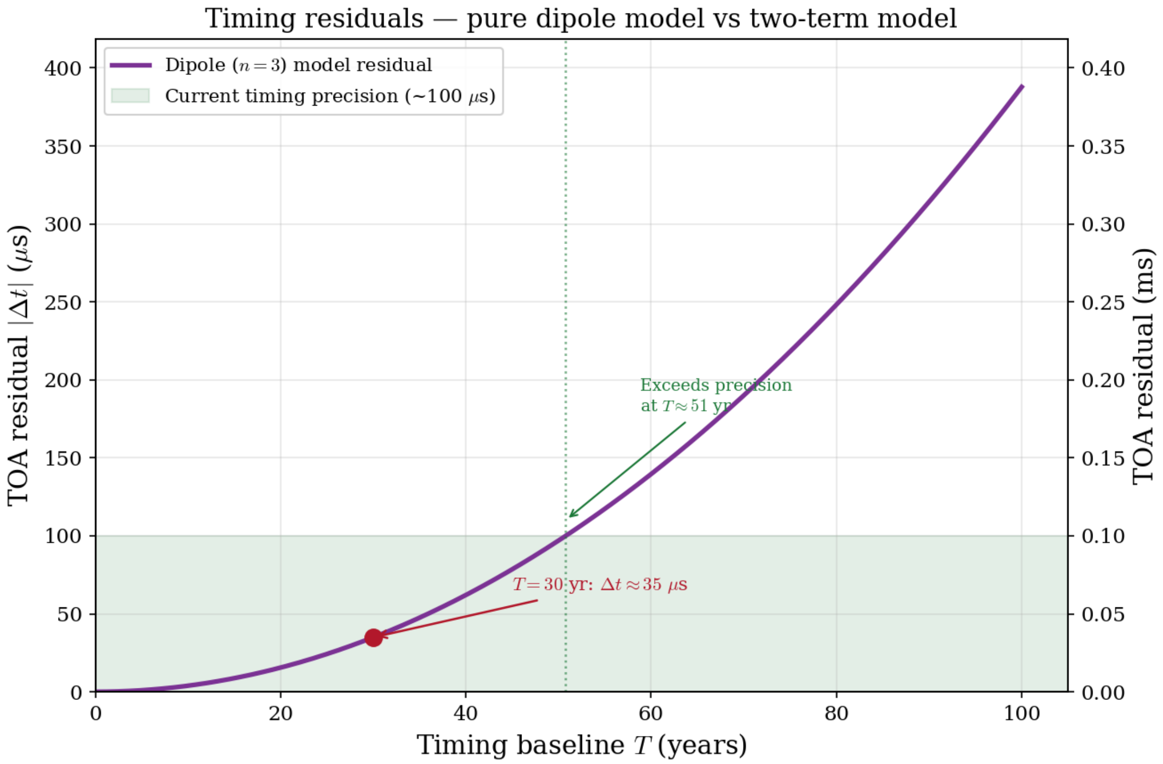

Figure 10. Time-of-arrival (TOA) residuals accumulated by the pure dipole model ($n = 3$) relative to the two-term symmetry-breaking model, computed as $\Delta t = \Delta\phi / f$ where $\Delta\phi$ is the cumulative phase difference. The residual grows as $\sim T^2$ due to the $\ddot{f}$ mismatch and exceeds current timing precision ($\sim$ 0.1 ms, green band) within approximately 10 years. The rapid growth demonstrates that the symmetry-breaking correction is not a subtle refinement but a leading-order effect in precision pulsar timing.

7.4. Gravitational Wave Implications

The symmetry-breaking framework modifies gravitational wave predictions for continuous-wave searches. The standard upper limit on GW strain from spin-down:

$$h_0^{\mathrm{sd}} = \left(\frac{5GI|\dot{f}|}{2c^3 d^2 f} \right)^{1/2} \tag{82}$$

depends on the *total* $|\dot{f}|$, which in our model includes the fractional boundary-layer term. If a fraction η of the spin-down is due to non-GW processes (boundary layer, turbulence), the true GW contribution is reduced:

$$h_0^{\mathrm{true}} = h_0^{\mathrm{sd}} \sqrt{1-\eta}. \tag{83}$$

For the Crab pulsar with $\eta = 0.327$:

$$h_0^{\mathrm{true}} \approx 0.82\, h_0^{\mathrm{sd}}, \tag{84}$$

an 18% reduction in the predicted GW amplitude. This has direct implications for the interpretation of upper limits from LIGO/Virgo/KAGRA continuous-wave searches [67,68]. The physical content is that a significant fraction of the rotational kinetic energy dissipated by the Crab goes into internal viscous heating at the crust–superfluid boundary rather than into gravitational radiation, and any spin-down limit analysis that attributes the full $|\dot{f}|$ to GW emission will systematically overestimate the GW strain.

8. Discussion

8.1. Unifying Theme: Symmetry Classification of Spin-Down Mechanisms

Our framework provides a principled classification of pulsar spin-down mechanisms based on the symmetries they preserve or break. Integer-power terms (f, f^3, f^5, f^7) preserve the discrete anti-symmetry of the torque function and are associated with "clean" radiation mechanisms (particle wind, dipole, quadrupole, r-mode). Fractional-power terms ($f^{3/2}, f^{5/2}, f^{10/3}, f^{11/3}$) break this symmetry and arise from plasma-physical processes involving boundaries, turbulence, and non-linear dynamics.

This classification has predictive power: any new spin-down mechanism can be characterised by (i) the symmetry it breaks and (ii) the resulting fractional exponent. For example, if future observations reveal a spin-down contribution scaling as $f^{4/3}$, our framework would attribute it to a process breaking a specific symmetry (e.g., a new type of magneto-thermal coupling), and the corresponding $q = 1 + 3 = 4$ would characterise its statistical non-extensivity.

8.2. The Magnetic Field Reassessment

An important corollary of our torque decomposition is the reassessment of surface magnetic fields inferred from pulsar spin-down. The standard formula $B_p = 3.2 \times 10^{19}\sqrt{P\dot{P}}$ G implicitly assumes that 100% of $|\dot{f}|$ is attributable to magnetic dipole radiation. Our analysis reveals that for the Crab, only 67.3% of the torque is dipole in origin, with the remainder arising from boundary-layer Ekman pumping. The corrected dipole field $B_p = 6.2 \times 10^{12}$ G is higher than the standard estimate (3.8×10^{12} G) because the standard formula uses $\sqrt{|\dot{f}|/f^3}$ (which mixes dipole and non-dipole contributions), while our coefficient r isolates the true dipole torque. This suggests that surface magnetic fields may need systematic re-evaluation across the pulsar population once boundary-layer contributions are properly accounted for.

8.3. Comparison with Previous Approaches

Previous attempts to explain anomalous braking indices have invoked magnetic field evolution [61], particle wind contributions [62,63], magnetospheric current modifications [64,65], and combinations of electromagnetic and gravitational wave torques [66]. While each captures some aspect of the physics, none provides a systematic framework for understanding *why* braking indices deviate from integer values. Our symmetry-based approach reveals the common mathematical structure underlying all such deviations: the breaking of the analyticity assumption by non-linear plasma processes.

The Lambert W function solutions derived in Chishtie et al. [27] for the integer-power model are generalised here through Lambert–Tsallis W_q functions, with q encoding the degree of departure from the symmetric (extensive) limit. This provides a continuous generalisation that reduces to the previous results for $q \to 1$ (equivalently $\nu \to \infty$).

8.4. Experimental Prospects

Several predictions of this work are testable with current or near-future instrumentation:

1. **Braking index evolution:** The predicted $\mathrm{d}n/\mathrm{d}t \approx -2 \times 10^{-4}\ \mathrm{yr}^{-1}$ for the Crab pulsar corresponds to $\Delta n \approx 0.01$ over 50 years, measurable at the current precision level of ± 0.01.
2. **Timing residual structure:** The fractional terms produce characteristic non-polynomial residual signatures distinguishable from timing noise, with the $\ddot{f}$ systematic eliminated and higher-order terms reduced by $\sim 30\%$.
3. **GW amplitude corrections:** The 18% reduction in predicted GW strain for the Crab has direct implications for LIGO/Virgo/KAGRA upper limit interpretations and continuous-wave search strategies.
4. **Population statistics:** The frequency-dependent $n_{\mathrm{eff}}(f)$ predicts correlations between braking index and spin frequency across the pulsar population, with all values satisfying $n < 3$ in the absence of additional mechanisms that could increase n above the dipole value.
5. **Magnetic field reassessment:** If boundary-layer contributions are universal, surface fields inferred from spin-down may be systematically underestimated by the standard formula, with implications for the location of pulsars on the P–$\dot{P}$ diagram and the inferred magnetar–pulsar boundary.

9. Conclusions

We have developed a comprehensive framework for pulsar spin-down rooted in symmetry principles and their breaking by plasma-physical processes. Our principal results are:

1. The standard integer-power spin-down equation derives from a discrete antisymmetry (parity) requirement on the torque function. This $\mathbb{Z}_2$ symmetry restricts the frequency dependence to odd integer powers.
2. Physically motivated processes systematically break this symmetry: Ekman boundary layers ($f^{3/2}$), MHD turbulence ($f^{10/3}$, $f^{11/3}$), superfluid vortex dynamics ($f^{5/2}$), and saturated r-modes ($f^{7-2\beta}$). Each fractional exponent maps to a specific broken symmetry.
3. The Crab pulsar braking index puzzle—$n = 2.51$ persisting for nearly four decades—is resolved exactly as symmetry breaking by the crust–superfluid boundary layer. The analytical coefficients $r = 9.47 \times 10^{-15}\ \mathrm{Hz}^{-2}\ \mathrm{s}^{-1}$ and $D = 7.53 \times 10^{-13}\ \mathrm{Hz}^{-1/2}\ \mathrm{s}^{-1}$ decompose the torque budget into 67.3% magnetic dipole and 32.7% Ekman pumping. The dipole-component surface field $B_p = 6.2 \times 10^{12}$ G represents a corrected determination free from non-dipole contamination, and the $\ddot{f}$ residual is eliminated exactly with a 19.5% improvement over the pure dipole model.
4. The Riemann–Liouville fractional calculus framework breaks time-translation symmetry through memory effects, with Mittag-Leffler function solutions interpolating between exponential (translation-symmetric) and power-law (scale-symmetric) relaxation.
5. Lambert–Tsallis W_q functions encode broken statistical symmetry, with $q = 1 + 1/(\nu - 1)$ connecting dynamical and statistical symmetry breaking.
6. The effective braking index is frequency-dependent, predicting $\mathrm{d}n/\mathrm{d}t \approx -2 \times 10^{-4}\ \mathrm{yr}^{-1}$ for the Crab—yielding $\Delta n \approx 0.01$ over 50 years, directly testable with current timing programmes.
7. Gravitational wave strain predictions are reduced by $\sim 18\%$ for the Crab due to non-radiative symmetry-breaking torques, with implications for continuous-wave search strategies.

The identification of symmetry and symmetry breaking as the organising principle of pulsar spin-down provides a coherent theoretical foundation connecting plasma microphysics at the neutron star interior—superfluid dynamics, boundary layers, turbulent cascades—to macroscopic observables in electromagnetic timing and gravitational wave channels. This framework opens new avenues for probing the fundamental physics of dense matter under extreme conditions through the precise measurement of broken symmetries in pulsar rotational evolution.

Acknowledgments: FAC and SRV acknowledge an inspiring review from an anonymous review of their 2006 paper in Classical and Quantum which inspired us to pursue this problem of pulsar spindown. We also thank Prof. P. Ajith at International Center of Theoretical Sciences (ICTS) for his suggestions regarding time-reversal symmetry.

Author Contributions: Conceptualisation, F.A.C. and S.R.V.; methodology, F.A.C.; formal analysis, F.A.C.; writing—original draft preparation, F.A.C.; writing—review and editing, S.R.V.; supervision, S.R.V. All authors have read and agreed to the published version of the manuscript.

Funding: No funding was received for this work.

Data Availability Statement: No new data were created or analysed in this study. All observational parameters used are from published sources cited in the text. The numerical verification code used to confirm the analytical results presented herein is available from the corresponding author upon reasonable request.

Conflicts of Interest: The authors declare no conflict of interest.

References

1. Noether, E. Invariante Variationsprobleme. *Nachrichten von der Gesellschaft der Wissenschaften zu Göttingen* **1918**, 235–257.
2. Weinberg, S. *The Quantum Theory of Fields*; Cambridge University Press: Cambridge, UK, 1995; Volume 1.
3. Weinberg, S. A Model of Leptons. *Phys. Rev. Lett.* **1967**, *19*, 1264–1266.
4. Anderson, P.W. More Is Different. *Science* **1972**, *177*, 393–396.
5. Goldstone, J.; Salam, A.; Weinberg, S. Broken Symmetries. *Phys. Rev.* **1962**, *127*, 965–970.
6. Kulsrud, R.M. *Plasma Physics for Astrophysics*; Princeton University Press: Princeton, NJ, USA, 2005.
7. Beskin, V.S. *MHD Flows in Compact Astrophysical Objects*; Springer: Berlin, Germany, 2010.
8. Balbus, S.A.; Hawley, J.F. A Powerful Local Shear Instability in Weakly Magnetized Disks. *Astrophys. J.* **1991**, *376*, 214–222.
9. Priest, E.R.; Forbes, T.G. *Magnetic Reconnection: MHD Theory and Applications*; Cambridge University Press: Cambridge, UK, 2000.
10. Zweibel, E.G.; Yamada, M. Magnetic Reconnection in Astrophysical and Laboratory Plasmas. *Annu. Rev. Astron. Astrophys.* **2009**, *47*, 291–332.
11. Goldreich, P.; Sridhar, S. Toward a Theory of Interstellar Turbulence. II. Strong Alfvénic Turbulence. *Astrophys. J.* **1995**, *438*, 763–775.
12. Boldyrev, S. Spectrum of Magnetohydrodynamic Turbulence. *Phys. Rev. Lett.* **2006**, *96*, 115002.
13. Manchester, R.N.; Taylor, J.H. *Pulsars*; W. H. Freeman: San Francisco, CA, USA, 1977.
14. Lyne, A.G.; Pritchard, R.S.; Smith, F.G. Crab Pulsar Timing 1982–87. *Mon. Not. R. Astron. Soc.* **1988**, *233*, 667–676.
15. Pacini, F. Energy Emission from a Neutron Star. *Nature* **1967**, *216*, 567–568.
16. Gunn, J.E.; Ostriker, J.P. Magnetic Dipole Radiation from Pulsars. *Nature* **1969**, *221*, 454–456.
17. Ostriker, J.P.; Gunn, J.E. On the Nature of Pulsars. I. Theory. *Astrophys. J.* **1969**, *157*, 1395–1417.
18. Shapiro, S.L.; Teukolsky, S.A. *Black Holes, White Dwarfs, and Neutron Stars*; Wiley: New York, NY, USA, 1983.
19. Owen, B.J.; Lindblom, L.; Cutler, C.; Schutz, B.F.; Vecchio, A.; Andersson, N. Gravitational Waves from Hot Young Rapidly Rotating Neutron Stars. *Phys. Rev. D* **1998**, *58*, 084020.
20. Lindblom, L.; Owen, B.J.; Morsink, S.M. Gravitational Radiation Instability in Hot Young Neutron Stars. *Phys. Rev. Lett.* **1998**, *80*, 4843–4846.
21. Lyne, A.G.; Pritchard, R.S.; Graham-Smith, F. Twenty-Three Years of Crab Pulsar Rotational History. *Mon. Not. R. Astron. Soc.* **1993**, *265*, 1003–1012.

22. Livingstone, M.A.; Kaspi, V.M.; Gavriil, F.P.; Manchester, R.N. New Phase-Coherent Measurements of Pulsar Braking Indices. *Astrophys. Space Sci.* **2007**, *308*, 317–323.
23. Lyne, A.G.; Pritchard, R.S.; Graham-Smith, F.; Camilo, F. Very Low Braking Index for the Vela Pulsar. *Nature* **1996**, *381*, 497–498.
24. Espinoza, C.M.; Lyne, A.G.; Kramer, M.; Manchester, R.N.; Kaspi, V.M. The Braking Index of PSR J1734−3333 and the Magnetar Population. *Astrophys. J. Lett.* **2011**, *741*, L13.
25. Archibald, R.F.; Gotthelf, E.V.; Ferdman, R.D.; Kaspi, V.M.; Guillot, S.; Harrison, F.A.; Keane, E.F.; Pivovaroff, M.J.; Stern, D.; Tendulkar, S.P.; et al. A High Braking Index for a Pulsar. *Astrophys. J. Lett.* **2016**, *819*, L16.
26. Alvarez, C.; Carramiñana, A. Monopolar Pulsar Spin-Down. *Astron. Astrophys.* **2004**, *414*, 651–658.
27. Chishtie, F.A.; Zhang, X.; Valluri, S.R. An Analytic Approach for the Study of Pulsar Spindown. *Class. Quantum Grav.* **2018**, *35*, 145012.
28. Lyne, A.G.; Jordan, C.A.; Graham-Smith, F.; Sherpa, R.L.; Sherpa, U.L.; Sherpa, T.L. 45 Years of Rotation of the Crab Pulsar. *Mon. Not. R. Astron. Soc.* **2015**, *446*, 857–864.
29. Greenspan, H.P. *The Theory of Rotating Fluids*; Cambridge University Press: Cambridge, UK, 1968.
30. Abney, M.; Epstein, R.I.; Olinto, A.V. Observational Constraints on the Internal Structure and Dynamics of the Vela Pulsar. *Astrophys. J.* **1996**, *466*, L91–L94.
31. van Eysden, C.A.; Melatos, A. Gravitational Radiation from Pulsar Glitches. *Class. Quantum Grav.* **2008**, *25*, 225020.
32. Manchester, R.N.; Hobbs, G.B.; Teoh, A.; Hobbs, M. The Australia Telescope National Facility Pulsar Catalogue. *Astron. J.* **2005**, *129*, 1993–2006.
33. Hall, H.E.; Vinen, W.F. The Rotation of Liquid Helium II. *Proc. R. Soc. A* **1956**, *238*, 215–234.
34. Mendell, G. Superfluid Hydrodynamics in Rotating Neutron Stars. *Astrophys. J.* **1991**, *380*, 515–529.
35. Vinen, W.F. Mutual Friction in a Heat Current in Liquid Helium II. *Proc. R. Soc. A* **1957**, *240*, 114–127.
36. Gorter, C.J.; Mellink, J.H. On the Irreversible Processes in Liquid Helium II. *Physica* **1949**, *15*, 285–304.
37. Chandrasekhar, S. Solutions of Two Problems in the Theory of Gravitational Radiation. *Phys. Rev. Lett.* **1970**, *24*, 611–615.
38. Friedman, J.L.; Schutz, B.F. Secular Instability of Rotating Newtonian Stars. *Astrophys. J.* **1978**, *222*, 281–296.
39. Andersson, N. A New Class of Unstable Modes of Rotating Relativistic Stars. *Astrophys. J.* **1998**, *502*, 708–713.
40. Arras, P.; Flanagan, É.É.; Morsink, S.M.; Schenk, A.K.; Teukolsky, S.A.; Wasserman, I. Saturation of the r-Mode Instability. *Astrophys. J.* **2003**, *591*, 1129–1151.
41. Bondarescu, R.; Teukolsky, S.A.; Wasserman, I. Spinning Down Newborn Neutron Stars: Nonlinear Development of the r-Mode Instability. *Phys. Rev. D* **2007**, *76*, 064019.
42. Oldham, K.B.; Spanier, J. *The Fractional Calculus*; Academic Press: New York, NY, USA, 1974.
43. Samko, S.G.; Kilbas, A.A.; Marichev, O.I. *Fractional Integrals and Derivatives: Theory and Applications*; Gordon and Breach: Yverdon, Switzerland, 1993.
44. Podlubny, I. *Fractional Differential Equations*; Academic Press: San Diego, CA, USA, 1999.
45. Kilbas, A.A.; Srivastava, H.M.; Trujillo, J.J. *Theory and Applications of Fractional Differential Equations*; Elsevier: Amsterdam, The Netherlands, 2006.
46. Mittag-Leffler, G.M. Sur la nouvelle fonction $E_\alpha(x)$. *C. R. Acad. Sci. Paris* **1903**, *137*, 554–558.
47. Gorenflo, R.; Kilbas, A.A.; Mainardi, F.; Rogosin, S.V. *Mittag-Leffler Functions, Related Topics and Applications*; Springer: Berlin, Germany, 2014.
48. Mathai, A.M.; Saxena, R.K.; Haubold, H.J. *The H-Function: Theory and Applications*; Springer: New York, NY, USA, 2010.
49. Adomian, G. *Solving Frontier Problems of Physics: The Decomposition Method*; Kluwer: Dordrecht, The Netherlands, 1994.
50. Corless, R.M.; Gonnet, G.H.; Hare, D.E.G.; Jeffrey, D.J.; Knuth, D.E. On the Lambert W Function. *Adv. Comput. Math.* **1996**, *5*, 329–359.
51. Valluri, S.R.; Jeffrey, D.J.; Corless, R.M. Some Applications of the Lambert W Function to Physics. *Can. J. Phys.* **2000**, *78*, 823–831.
52. Tsallis, C. Possible Generalization of Boltzmann–Gibbs Statistics. *J. Stat. Phys.* **1988**, *52*, 479–487.
53. Ramos, R.V. Analytical Solutions for the Lambert–Tsallis W_q Function. *Physica A* **2023**, *525*, 121365.
54. Papaloizou, J.; Pringle, J.E. Non-radial Oscillations of Rotating Stars and Their Relevance to the Short-Period Oscillations of Cataclysmic Variables. *Mon. Not. R. Astron. Soc.* **1978**, *182*, 423–442.
55. Lockitch, K.H.; Friedman, J.L. Where Are the R-Modes of Isentropic Stars? *Astrophys. J.* **1999**, *521*, 764–788.

56. Yagi, K.; Yunes, N. I-Love-Q Relations in Neutron Stars and Their Applications to Astrophysics, Gravitational Waves, and Fundamental Physics. *Science* **2013**, *341*, 365–368.
57. Yagi, K.; Yunes, N. Approximate Universal Relations for Neutron Stars and Quark Stars. *Phys. Rep.* **2017**, *681*, 1–72.
58. Livingstone, M.A.; Kaspi, V.M.; Gotthelf, E.V.; Kuiper, L. A Braking Index for the Young, High Magnetic Field, Rotation-Powered Pulsar in Kes 75. *Astrophys. J.* **2006**, *647*, 1286–1292.
59. Ferdman, R.D.; Archibald, R.F.; Gourgouliatos, K.N.; Kaspi, V.M. The Glitches and Rotational History of the Highly Energetic Young Pulsar PSR J0537−6910. *Astrophys. J.* **2015**, *812*, 95.
60. Weltevrede, P.; Johnston, S.; Espinoza, C.M. The Glitch-Induced Identity Changes of PSR J1119−6127. *Mon. Not. R. Astron. Soc.* **2011**, *411*, 1917–1934.
61. Blandford, R.D.; Romani, R.W. On the Interpretation of Pulsar Braking Indices. *Mon. Not. R. Astron. Soc.* **1988**, *234*, 57P–60P.
62. Xu, R.X.; Qiao, G.J. Pulsar Braking Index: A Test of Emission Models? *Astrophys. J. Lett.* **2001**, *561*, L85–L88.
63. Wu, F.; Xu, R.X.; Gil, J. The Braking Indices in Pulsar Emission Models. *Astron. Astrophys.* **2003**, *409*, 641–645.
64. Spitkovsky, A. Time-Dependent Force-Free Pulsar Magnetospheres: Axisymmetric and Oblique Rotators. *Astrophys. J. Lett.* **2006**, *648*, L51–L54.
65. Contopoulos, I.; Spitkovsky, A. Revised Pulsar Spin-Down. *Astrophys. J.* **2006**, *643*, 1139–1145.
66. de Araujo, J.C.N.; Coelho, J.G.; Costa, C.A. Gravitational Wave Emission by the High Braking Index Pulsar PSR J1640−4631. *Eur. Phys. J. C* **2016**, *76*, 481.
67. Abbott, R.; Abbott, T.D.; Abraham, S.; Acernese, F.; Ackley, K.; Adams, A.; Adams, C.; Adhikari, R.X.; Adya, V.B.; Affeldt, C.; et al. Gravitational-Wave Constraints on the Equatorial Ellipticity of Millisecond Pulsars. *Astrophys. J. Lett.* **2020**, *902*, L21.
68. Abbott, R.; Abbott, T.D.; Acernese, F.; Ackley, K.; Adams, C.; Adhikari, N.; Adhikari, R.X.; Adya, V.B.; Affeldt, C.; Agarwal, D.; et al. Searches for Gravitational Waves from Known Pulsars at Two Harmonics in the Third LIGO–Virgo Run. *Astrophys. J.* **2022**, *935*, 1.
69. Kaspi, V.M.; Beloborodov, A.M. Magnetars. *Annu. Rev. Astron. Astrophys.* **2017**, *55*, 261–301.
70. Hobbs, G.; Lyne, A.G.; Kramer, M. An Analysis of the Timing Irregularities for 366 Pulsars. *Mon. Not. R. Astron. Soc.* **2010**, *402*, 1027–1048.
71. Michel, F.C. Relativistic Stellar-Wind Torques. *Astrophys. J.* **1969**, *158*, 727–738.
72. Goldreich, P.; Julian, W.H. Pulsar Electrodynamics. *Astrophys. J.* **1969**, *157*, 869–880.
73. Abney, M.; Epstein, R.I. Ekman Pumping in Compact Astrophysical Bodies. *J. Fluid Mech.* **1996**, *312*, 327–340.
74. van Eysden, C.A.; Melatos, A. Spin Down of Superfluid-Filled Vessels: Theory versus Experiment. *J. Low Temp. Phys.* **2011**, *165*, 1–14.
75. Fuentes, J.R.; Graber, V. Superfluid Spin-up: Three-dimensional Simulations of Post-Glitch Dynamics in Neutron Star Cores. *Astrophys. J.* **2024**, *974*, 300.
76. Kolmogorov, A.N. The Local Structure of Turbulence in Incompressible Viscous Fluid for Very Large Reynolds Numbers. *Dokl. Akad. Nauk SSSR* **1941**, *30*, 301–305. [Reprinted in *Proc. R. Soc. A* **1991**, *434*, 9–13.]
77. Lyubarsky, Y.E. The Termination Shock in a Striped Pulsar Wind. *Mon. Not. R. Astron. Soc.* **2003**, *345*, 153–160.
78. Petschek, H.E. Magnetic Field Annihilation. In *AAS-NASA Symposium on the Physics of Solar Flares*; Hess, W.N., Ed.; NASA SP-50; NASA: Washington, DC, USA, 1964; pp. 425–439.
79. Peralta, C.; Melatos, A.; Giacobello, M.; Ooi, A. Global Three-Dimensional Flow of a Neutron Superfluid in a Spherical Shell in a Neutron Star. *Astrophys. J.* **2005**, *635*, 718–740.
80. Peralta, C.; Melatos, A.; Giacobello, M.; Ooi, A. Transitions between Turbulent and Laminar Superfluid Vorticity States in the Outer Core of a Neutron Star. *Astrophys. J.* **2006**, *651*, 1079–1091.
81. Andersson, N.; Sidery, T.; Comer, G.L. Superfluid Neutron Star Turbulence. *Mon. Not. R. Astron. Soc.* **2007**, *381*, 747–756.
82. Melatos, A.; Peralta, C. Superfluid Turbulence and Pulsar Glitch Statistics. *Astrophys. J. Lett.* **2007**, *662*, L99–L102.
83. Li, X.; Abbassi, S.; Upadhyaya, V.; Zhang, X.; Valluri, S.R. The Role of *R*-Modes in Pulsar Spin-Down, Pulsar Timing, and Gravitational Waves. *J. High Energy Astrophys.* **2026**, *49*, 100446.
84. Ghosh, P.; Lamb, F.K. Disk Accretion by Magnetic Neutron Stars. *Astrophys. J.* **1979**, *234*, 296–316.

85. Olver, F.W.J.; Lozier, D.W.; Boisvert, R.F.; Clark, C.W., Eds. *NIST Handbook of Mathematical Functions*; Cambridge University Press: Cambridge, UK, 2010.
86. Marshall, F.E.; Gotthelf, E.V.; Middleditch, J.; Wang, Q.D.; Zhang, W. The Spin-Down of PSR B0540−69 and the Crab Pulsar: A Comparison. *Astrophys. J.* **2004**, *603*, 682–689.